Remote Sensing of Environment 253 (2021) 112202

Contents lists available at ScienceDirect

Remote Sensing of Environment

journal homepage: www.elsevier.com/locate/rse

A scattering law based cirrus correction method for Landsat 8 OLI visible and near-infrared images

Chi Zhang [a], Huifang Li [a,*], Huanfeng Shen [a,b,c]

[a] School of Resource and Environmental Sciences, Wuhan University, PR China
[b] The Collaborative Innovation Center for Geospatial Technology, PR China
[c] The Key Laboratory of Geographic Information System, Ministry of Education, Wuhan University, PR China

ARTICLE INFO

Keywords:
Cirrus correction
Scattering law
Band correlation
Landsat 8 OLI images

ABSTRACT

Cirrus clouds are commonly distributed in the atmosphere, and can lead to degradation of the ground information in optical remotely sensed images obtained using airborne and spaceborne sensors. A cirrus band on the Landsat 8 Operational Land Imager (OLI), i.e., Band 9, is designed to precisely detect cirrus cloud, providing a reference basis for the radiance calculation of cirrus cloud in other bands. Therefore, based on a scattering law, a cirrus cloud correction method is proposed in this paper to restore the ground information for Landsat 8 OLI visible and near-infrared (VNIR) images by comprehensively using the visible and cirrus bands. The scattering law and the high correlation between the two adjoining blue bands are combined to estimate each VNIR band's cirrus radiance. The relationship among the bands is constrained to comply with the scattering law. The differences between the ocean and land surfaces are also considered when determining the parameter in the scattering law. In the experiments conducted in this study, both simulated and acquired images contaminated with cirrus cloud were used to evaluate the proposed method, and both visual and quantitative evaluations were carried out to verify the performance. The results suggest that the cirrus cloud in the VNIR bands can be removed by the use of the proposed method. The ground information can also be adequately restored, with a mean absolute error of less than 0.7757 for the simulated data and a structural similarity index measure of greater than 0.8621 for the acquired data. When compared with three existing correction methods, the proposed method was able to obtain clearer and more accurate results over various land and ocean scenes. Furthermore, this method's applicability to other sensors with similar bands, such as the Sentinel-2 Multispectral Instrument, was also investigated and validated.

1. Introduction

Ground radiation travels a long distance and interacts with the turbid medium in the atmosphere before reaching satellite sensors at orbits of around 600–900 km in altitude, which can cause ground radiation distortion or loss. Cirrus is a typical turbid state of the atmosphere, covering approximately 30% of the global surface and 50% in mid-latitude and tropical regions (Chepfer et al., 2000). To restore the ground information beneath the cirrus cloud, one needs to correct the cirrus cloud from optical remote sensing images.

Cirrus cloud is typically characterized by thin and wispy strands in the sky (McFarquhar and Heymsfield, 1997; Gao et al., 1998). Meanwhile, it is generally semi-transparent in visible and near-infrared (VNIR) remote sensing images and can be categorized as a type of thin cloud (Gao and Li, 2000; Lv et al., 2019; Makarau et al., 2016). Several thin cloud removal methods have been proposed, utilizing the statistical information from the spatial, spectral, and frequency domains, including the dark object subtraction based methods (Chavez Jr, 1988; Makarau et al., 2014; Vincent, 1972), image transformation based methods (Chen et al., 2016; He et al., 2010; Lv et al., 2016; Zhang et al., 2002; Crist and Cicone, 1984; Shen et al., 2015), and filtering in the frequency domain (Chanda and Majumder, 1991; Du et al., 2002; Liu et al., 2014; Shen et al., 2014). Nevertheless, few methods can estimate the intensity of thin clouds precisely in the VNIR bands. An important reason for this is that thin clouds are usually a mixture of different clouds whose characteristics are complicated and varied. It is reasonable to aim at one type of cloud if precise quantitative correction is required. We aimed to correct the cirrus cloud in this study because it has unique

* Corresponding authors at: School of Resource and Environmental Sciences, Wuhan University, PR China.
E-mail addresses: zhangchi9502@outlook.com (C. Zhang), huifangli@whu.edu.cn (H. Li), shenhf@whu.edu.cn (H. Shen).

https://doi.org/10.1016/j.rse.2020.112202
Received 17 October 2019; Received in revised form 13 November 2020; Accepted 16 November 2020
Available online 3 December 2020

characteristics in certain water vapor absorption bands and atmospheric vertical columns, which can benefit the correction.

With the difference from other clouds, cirrus cloud is mainly made up of ice crystals and some other small particles, such as gas molecules of approximately 0.1–0.2 nm. The ice crystals suspended in cirrus cloud are of various shapes and are typically 5 μm or greater (Gao and Li, 2012; Lucke et al., 2011). The atmospheric layer beneath the cirrus cloud aggregates most of the water vapor in the atmosphere (Gao et al., 2002). Thus, for a narrow band near the water vapor absorbing spectra, e.g., 1.38 μm, when there is abundant water vapor or moisture between the ground target and the airborne or satellite sensor, the upward ground radiation will be absorbed entirely. Still, the scattered radiation from the cirrus cloud can be well recorded by the sensor (Gao et al., 1998). Narrow bands (hereafter referred to as "cirrus bands") can be used to detect cirrus cloud and can be used for cirrus correction (Gao et al., 1998). Cirrus bands are now assigned in many satellite sensors, such as Band 9 (1.363–1.384 μm) of the Operational Land Imager (OLI) onboard the Landsat 8 satellite (Zanter, 2016), Band 26 (1.36–1.39 μm) of the Moderate Resolution Imaging Spectroradiometer (MODIS) onboard the Terra and Aqua satellites (Dessler and Yang, 2003), and Band 10 (1.36–1.39 μm) of the Multispectral Instrument (MSI) onboard the Sentinel-2 satellite (Drusch et al., 2012).

In recent decades, several cirrus correction methods using cirrus bands have been developed. Generally speaking, the intensity of the cirrus cloud in the various bands is estimated by fitting the cloudy bands with the cirrus bands using a linear or nonlinear regression (Gao and Li, 2017; Gao et al., 2002; Gao et al., 1998; Shen et al., 2015; Xu et al., 2014). For example, Gao et al. (1998) proposed a pioneering method for hyperspectral images captured by the Airborne Visible Infrared Imaging Spectrometer (AVIRIS) in the late 1990s, in which the band near 1.38 μm was paired with the bands near 1.24 μm and 0.66 μm to correct cirrus cloud over water and land surfaces in the bands at the spectral range of 0.4–1.0 μm. As similar bands are available for MODIS, the same technique was incorporated in the first-generation MODIS atmospheric correction algorithms (Gao et al., 1998; Meyer et al., 2004). However, the requirements for bands and samples limit the extension of this method to other data and scenes. For the Landsat 8 OLI sensor, the linear relationships between the cirrus band (Band 9) and cloudy bands have been used to estimate and correct cirrus cloud (Gao and Li, 2017; Xu et al., 2014). However, the requirement for linear band correlation cannot be satisfied unless dark and homogeneous surfaces exist in the images. From the image transformation aspect, Shen et al. (2015) developed an independent component analysis (ICA) based method for correcting the thin cloud in OLI images, but the transformed component cannot describe cirrus cloud precisely, and the physical basis is insufficiently clear. In summary, the current cirrus correction methods mainly use the regression relationship between the cloudy VNIR bands and a cirrus band, which is an approach that is usually effective for simple homogeneous areas but is limited for other complex scenes. Moreover, the estimation of the cirrus intensity in each VNIR band is independent and the band correlation is ignored, which often leads to spectral distortion in the corrected results.

In this paper, we propose a cirrus correction method with high spatial and spectral fidelity for OLI VNIR images by using the cirrus band and constraining the VNIR band correlation with a scattering law. The rest of this paper is arranged as follows. Section 2 introduces the data and the cloudy image model. Section 3 provides details of the proposed scattering law based cirrus correction method. Section 4 describes the experiments undertaken with Landsat 8 OLI and Sentinel-2 MSI images covering different land surfaces to verify the effectiveness and robustness of the proposed method. Section 5 discusses the applicability of the method to other sensors with similar bands and the limitation of the method. Section 6 concludes the paper.

2. Data and model

2.1. Landsat 8 OLI images

The Landsat 8 satellite was launched in February 2013 with the OLI instrument onboard, which can record the Earth's surface in the visible and infrared spectral ranges. Compared with previous Landsat sensors, the OLI sensor has two new bands: Band 1 and Band 9. Band 1 is a deep blue visible band at 0.435–0.451 μm, which is specifically designed for coastal zone investigation, so this band is also called the "coastal band". Band 9 is a cirrus band with spectral range of 1.363–1.384 μm, which can detect cirrus cloud at a 30-m spatial resolution (Zanter, 2016).

2.2. Cloudy image model

An observed VNIR cloudy image can be simply modeled as follows (Chavez Jr, 1988; Makarau et al., 2014; Xia et al., 2018):

$$I_i^* = I_i + C_i \tag{1}$$

where I^* is the apparent radiance recorded by the sensor, I indicates the ground radiance underneath the cirrus cloud, and C is the radiance caused by the cirrus cloud. i is the index of bands, ranging from 1 to 5, covering the VNIR spectra of the OLI sensor. To obtain the cloud-free I, we need to estimate the corresponding cirrus cloud radiance C. Similar to I^* and I, C is a wavelength-dependent variable, which is the key to restoring the ground information with high fidelity from Eq. (1).

In VNIR bands, the cirrus cloud radiance is mainly caused by scattering, and not absorption (Gao et al., 1998). For a cirrus-covered pixel with a certain area in an image, different scattering types can simultaneously occur in that region, depending on the relationship between the particle size and the wavelength. Concretely, for particles with sizes much smaller than the wavelength, such as gas molecules, Rayleigh scattering is triggered. For particles with sizes comparable to or larger than the wavelength, the scattering type is Mie scattering. As the particle sizes increases and becomes much larger than the wavelength, optical scattering occurs. That is, the cirrus radiance C in a pixel is a mixture of multiple scatterings, which is band-dependent, and a mixed scattering law is defined to describe this in this paper. The aim of the proposed method is to calculate the band-dependent cirrus radiance and correct it from the observed VNIR images.

3. Methodology

A method based on a scattering law is constructed to calculate and correct each VNIR band's cirrus cloud radiance. Land and ocean surfaces are separately considered, according to their different radiometric characteristics.

3.1. Scattering law for cirrus cloud

As described in Section 2.2, mixed scattering occurs in cirrus pixels, and the cirrus radiance depends on the wavelength. Modeling the cirrus radiance caused by the mixed scattering is the physical basis used to explore the difference and correlation among bands. According to Chavez Jr (1988, 1989), the cloud radiance caused by the mixed scattering can be described by a scattering law. This law suggests that the scattered cloud radiance in a band can be simply modeled as a function related to the wavelength and several atmospheric property related

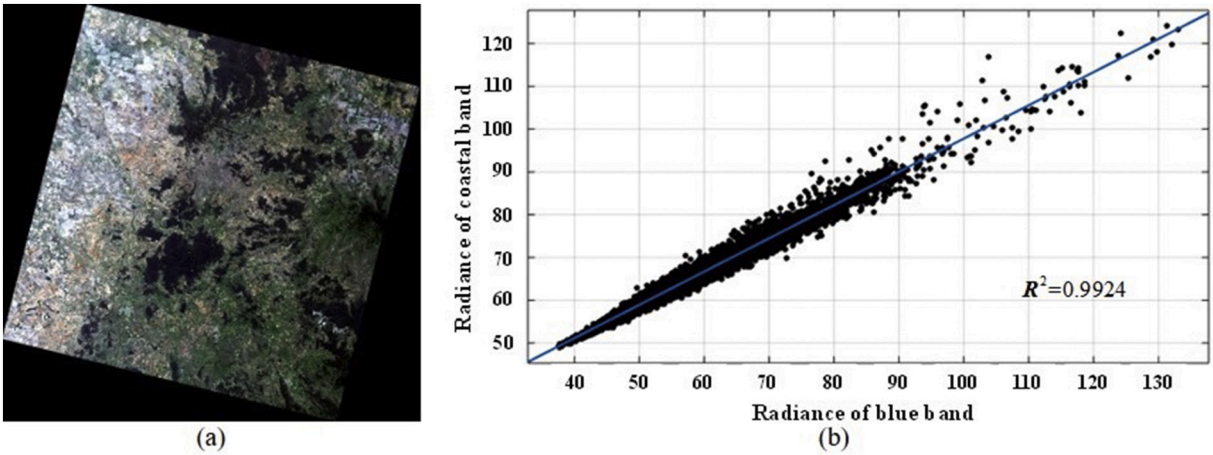

Fig. 1. An example OLI image of a clear land area and the corresponding scatterplot. (a) True-color image. (b) Scatterplot of the coastal and blue band radiance. (For interpretation of the references to color in this figure legend, the reader is referred to the web version of this article.)

parameters, which can be described as follows (Bucholtz, 1995; Li et al., 2012; McCartney, 1976):

$$C_i = D \cdot \lambda_i^{-\gamma} \tag{2}$$

where the subscript i denotes the ith band of the multispectral image; λ represents the wavelength; D is a variable describing the atmospheric properties at the imaging instant; and γ is a scattering-related parameter, depending on the relationship between the particle size and the wavelength, with its dynamic range being [0, 4] (Chavez Jr, 1988). When the atmosphere is very pure and clear, the particles in the atmosphere are mainly gas molecules that are much smaller than the wavelength, Rayleigh scattering is dominant, and γ equals 4, ideally. When the atmosphere becomes cloudy, not only the small particles but also others with sizes comparable to or larger than the wavelength exist, so that the scattering is a mixture of multiple scattering types, and γ equals a value between 0 and 4. Eq. (2) is restricted to Bands 1–5 and 9 of the OLI sensor, in which scattering effect is the dominant for cirrus cloud.

For a certain pixel, the atmosphere status is spatially identical, and thus, γ and D can be considered as constants in Bands 1–5 and 9 for the OLI sensor. Therefore, if the cloud radiance of band i is known, the cloud radiance of band j can be derived as follows:

$$C_j = \left(\frac{\lambda_i}{\lambda_j}\right)^{\gamma} \cdot C_i \tag{3}$$

where i and j are a pair of band indices between the VNIR and cirrus bands. For OLI data, the ground radiance in the cirrus band I_9 is nearly equal to 0 in most cases, so the apparent radiance I_9* can be regarded as the cirrus radiance C_9, i.e., $C_9 = I_9$*. Therefore, on the basis of Eq. (3), the cirrus radiance of the VNIR bands can be calculated by taking C_9 as a reference when γ is known. The γ value for a clear region is considered to be 4, but the problem is then how to obtain parameter γ over cirrus cloud regions. The cirrus band is used to discriminate clear regions from cirrus cloud regions.

3.2. Parameter γ determination for different cloudy surfaces

Land and ocean surfaces show distinctly different radiometric characteristics, which makes the means to determine γ for these two cloudy surfaces different. Over cloudy land surfaces, γ is determined based on the high linear correlation between the coastal and blue bands, while over cloudy ocean surfaces, it is determined by utilizing the regional stability of the atmosphere.

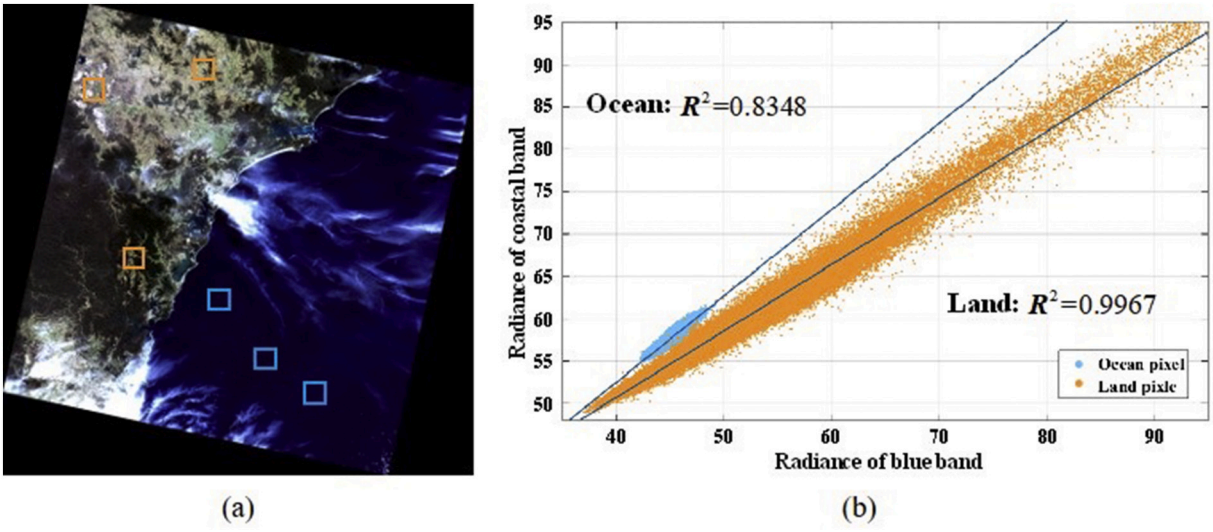

Fig. 2. An example OLI image of a coastal area and the corresponding scatterplot. (a) True-color image. (b) Scatterplot of coastal band versus blue band over land and ocean surfaces. (For interpretation of the references to color in this figure legend, the reader is referred to the web version of this article.)

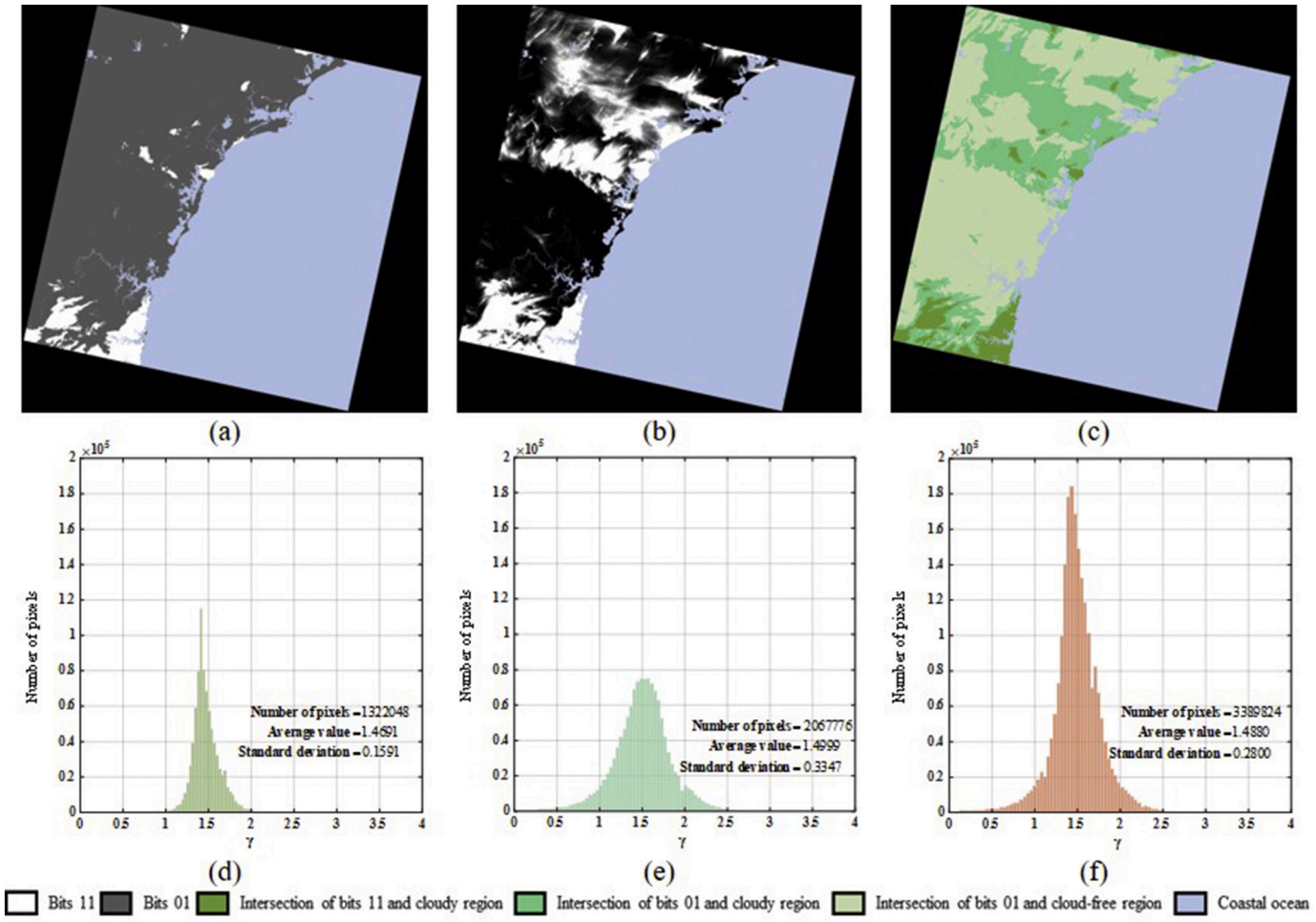

Fig. 3. Statistical results of γ for cloudy pixels with different cirrus bits in the QA band. (a) Visualization of the QA band over land surfaces, where the gray and white colors respectively represent cirrus bits 01 and 11, and the blue color indicates the ocean surfaces. (b) Cirrus band over land surfaces, in which the blue color indicates ocean surfaces. (c) Intersection areas of pixels with bits 11 and cloudy regions (dark green color), bits 01 and cloudy regions (green color), and bits 01 and cloud-free regions (light green color). (d) The γ histogram of pixels in the dark green regions. (e) The γ histogram of pixels in the green regions. (f) The γ histogram of all the cloudy pixels. (For interpretation of the references to color in this figure legend, the reader is referred to the web version of this article.)

3.2.1. Determination over cloudy land surfaces

The coastal and blue bands of the OLI sensor are located in the range of 0.435–0.451 μm and 0.452–0.512 μm, respectively, which are very close, with both belonging to the blue spectrum (Zanter, 2016). Under a clear sky, the ground radiance of the various cover types in these two bands are assumed to be linearly related over land, which can be expressed as follows:

$$I_1 = a \cdot I_2 + b \tag{4}$$

where subscripts 1 and 2 denote the coastal and blue bands of the OLI sensor, respectively. a and b are the regression coefficients obtained by fitting the clear pixels in the cirrus cloud images.

A clear land OLI image with various land-cover types (path: 91; row: 82) acquired on February 13, 2016, in Mendooran, Australia, was selected as an example to testify the assumption, as shown in Fig. 1a. The radiance of the coastal band versus the blue band for all the pixels in the scene is plotted in Fig. 1b, where the determination coefficient ($\mathbf{R^2}$) of the linear fitting is equal to 0.9924. The linear correlation is very strong for the various land covers, thus confirming the assumption.

Combining Eqs. (1), (3), and (4), a single equation set solving γ for cloudy land surfaces is derived:

$$\begin{cases} I_1^* = I_1 + C_1 \\ I_2^* = I_2 + C_2 \\ I_1 = a \cdot I_2 + b \\ C_1 = \left(\dfrac{\lambda_9}{\lambda_1}\right)^{\gamma} \cdot C_9 \\ C_2 = \left(\dfrac{\lambda_9}{\lambda_2}\right)^{\gamma} \cdot C_9 \end{cases} \tag{5}$$

In Eq. (5), there are five unknown variables, namely, I_1, I_2, C_1, C_2, and γ, which are equal to the number of equations. Thus, over land surfaces, the corrected cloud-free images of the coastal and blue bands can be obtained while the key parameter γ is solved.

3.2.2. Determination over cloudy ocean surfaces

Oceans are rich in sediments, suspended chlorophyll-rich phytoplankton, and other organic matter (Slonecker et al., 2016), which is evidently different from the land composition. The coastal band is the only one that is sensitive to the materials in oceans, whereas the blue band is not (Loyd, 2013). This makes the fitting coefficients and

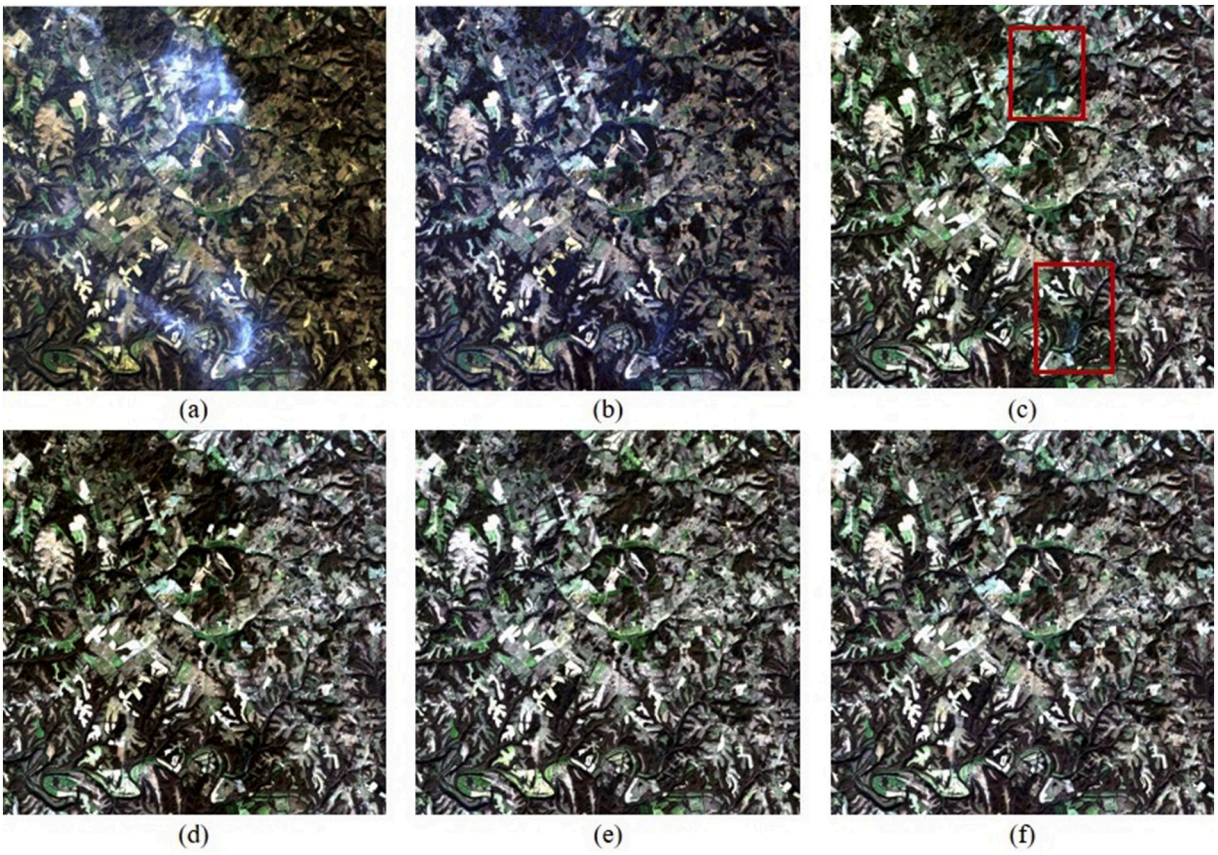

Fig. 4. Results for the simulated cirrus cloud image with complex land-cover types. (a) Simulated cirrus image. (b) ICARM. (c) ACRM. (d) ECCM. (e) Proposed method. (f) Ground truth.

correlations in Eq. (4) for ocean and land surfaces different.

A typical OLI image of a coastal area acquired on October 04, 2013, covering land and ocean surfaces was used to testify the linear relationship, as shown in Fig. 2. The primary land covers of the image are ocean surface, mudflat, forest, and bare land. Clear samples of land and ocean surfaces are marked by the orange and blue rectangles, respectively, in Fig. 2a, and the corresponding scatterplot in the coastal-blue space is shown in Fig. 2b. The clear ocean and land samples both show a significant linear correlation, but different fitting coefficients. Moreover, the radiance dynamic range is broad for the land surface but compact for the ocean surface, which leads to unreliable fitting. The $\mathbf{R^2}$ is 0.9967 for the land surface and 0.8348 for the ocean surface, which is clearly lower than for the land surface. If the linear relationship over the ocean surface is directly substituted into Eq. (5), γ will be misestimated, suggesting that the separate linear regression is infeasible and that an alternative strategy is required.

As the atmosphere is regionally homogeneous, the scattering effect in a local region can be supposed to be spatially consistent, which means that the scattering-related parameter γ can be shared for that region. We again take Fig. 2a as an example to analyze the dynamic range of γ values over cloudy land surfaces, in which pixels with different bits in the quality assessment (QA) band are separated. Fig. 3a shows a visualization of the QA band over land surfaces (with the coastal ocean masked by the blue color), in which there are pixels with bits 11 (white color) and bits 01 (gray color), and no pixels with bits 10 exist. Bits 11 and 01 respectively represent that there is high confidence (67–100%) and low to no confidence (0–33%) that cirrus exists. The corresponding cirrus band over land surfaces is shown in Fig. 3b, from which the cloudy regions with high values can be recognized easily. Comparing Fig. 3a and b, it can be seen that the cloudy regions are formed by all the pixels with bits 11 and some of the pixels with bits 01 in the QA band. The intersection areas of pixels with bits 11 and cloudy regions, bits 01 and cloudy regions, and bits 01 and cloud-free regions are colored in dark green, green, and light green, respectively, in Fig. 3c. The γ histograms of pixels in the dark green and green regions are shown in Fig. 3d and Fig. 3e, respectively, and Fig. 3f shows the γ histogram of all the cloudy pixels. The average and maximum values of γ for those pixels with bits 11 are 1.4691 and 2.1500, respectively, and those for cloudy pixels with bits 01 are greater, i.e., 1.4999 and 3.1373, respectively, indicating that the more cloudy a pixel is, the smaller the corresponding γ value will be. The standard deviations of cloudy pixels with bits 11 and 01 are 0.1591 and 0.3347, respectively, which are small values. Moreover, on the basis of the γ histogram for all the cloudy pixels in Fig. 3f, the pixels locating within one standard deviation from the average γ value account for nearly 80%, confirming that γ is a regionally stable variable. This enables us to transfer the γ values of land surfaces to the neighboring ocean surfaces. Therefore, we take the average of the γ values over the cloudy land surfaces as a common value over the cloudy ocean surfaces. The cirrus cloud radiance in the VNIR bands can then be calculated and finally removed from the ocean surface. In the experimental section, multiple coastal images with cirrus cloud are used to verify the practicability of the parameter determination approach for ocean surfaces.

3.3. Cirrus correction

Once the γ values for different surfaces are obtained, the band-

Table 1
Quantitative assessment of the results of the cirrus correction over a land area.

			ICARM	ACRM	ECCM	Proposed
RMSE	Cloudy area	Band 1	7.8399	3.5229	4.6302	1.2856
		Band 2	8.2232	3.5050	4.1513	1.3650
		Band 3	5.5662	2.4574	2.4859	0.7194
		Band 4	3.9949	1.7975	1.5508	0.3905
		Band 5	2.2159	5.0858	0.3058	0.1140
	Full scene	Band 1	7.1799	3.4462	4.5239	1.3146
		Band 2	7.5895	3.4288	4.0584	1.3452
		Band 3	5.1113	2.4025	2.4302	0.7121
		Band 4	3.6587	1.7564	1.5157	0.3880
		Band 5	2.0244	4.9595	0.2963	0.1141
MAE	Cloudy area	Band 1	7.4860	2.9650	3.9631	0.6880
		Band 2	7.8880	2.9504	3.5637	0.7736
		Band 3	5.3274	2.0560	2.1336	0.4197
		Band 4	3.8116	1.4936	1.3298	0.2334
		Band 5	2.1063	4.0700	0.1667	0.0708
	Full scene	Band 1	6.8249	2.8657	3.8091	0.6734
		Band 2	7.2421	2.8519	3.4335	0.7757
		Band 3	4.8664	1.9824	2.0552	0.4227
		Band 4	3.4755	1.4366	1.2800	0.2360
		Band 5	1.9179	3.8744	0.1502	0.0721
SA	Cloudy area	/	3.2417	7.1842	2.0060	0.4971
	Full scene	/	2.8958	6.6898	1.5312	0.4830

Note: Underline means that all bands were used to calculate the metric value.

dependent cirrus cloud radiance can be calculated by taking the cirrus band as the basis via Eq. (3). The corrected images can then be yielded by subtracting the cirrus cloud radiance from the observed images, i.e.,

$$I_i = I_i^* - C_i \tag{6}$$

where i ranges from 1 to 5, namely, the VNIR bands of the OLI.

Since the cirrus radiance in the VNIR bands is calculated with the constraint of a scattering law, the difference and correlation among bands are both considered, and the correction results should have high spectral fidelity with the ground truth, which is verified in the next section.

4. Results

Two simulated and nine acquired Landsat 8 OLI images with cirrus cloud were collected from land and coastal regions to validate the effectiveness of the proposed cirrus correction method. Three existing cirrus correction methods were selected and tested for comparison, i.e., the ICA based cirrus removal method (ICARM) (Shen et al., 2015), an automatic cloud removal method (ACRM) (Xu et al., 2014), and the empirical cirrus correction method (ECCM) (Gao and Li, 2017). Taking the temporally adjacent cloud-free images as reference, visual and quantitative assessments were performed to evaluate the results. Moreover, two Sentinel-2 MSI images from coastal and land areas were collected to further validate the applicability of the method to other sensors.

4.1. Analyses and results using simulated datasets

The simulated cirrus images were generated based on the cloudy image model and the scattering law, as expressed in Eqs. (1) and (2). In practice, I was the ground truth from a clear image, the Band 9 of a real image with cirrus was selected as the reference basis of C, and the γ values were set to vary within a small range of [0, 4] for cloudy regions and were set to 4 for clear regions.

4.1.1. Cirrus correction over land areas

Fig. 4a shows a simulated cirrus image of a land area, which is composed mainly of farmland, forest, and bare land. Fig. 4b–e present the results of ICARM, ACRM, ECCM, and the proposed method. The ground truth is shown in Fig. 4f. Visually, most of the cirrus can be removed by the ICARM method, but residual cirrus remains, and the color is clearly different from the cloud-free reference image in both the cloudy and clear regions. The results of the ACRM and ECCM methods show evident spectral differences between the corrected cloudy regions and the original clear regions. Furthermore, the region with dense cirrus cannot be fully corrected, and the color tends to be blue in the result of the ACRM method, as shown in the red rectangles in Fig. 4c. Among these results, Fig. 4e is the closest to the reference ground truth in Fig. 4f, for both the spatial distribution and displayed color.

Three metrics, i.e., the root-mean-square error (RMSE), mean absolute error (MAE), and spectral angle (SA), were calculated for the cloudy area and the full scene, to quantitatively evaluate the results. Table 1 lists the statistical results for these metrics, in which the RMSE and MAE were calculated for each band, and the SA was calculated for multiple bands. The smaller the metric value, the better the result. As indicated by the table, the proposed method performs the best in all the metrics for all the VNIR bands, which is consistent with the visual evaluation. For the ICARM and ACRM methods, the SA values are large, indicating that they are weak in preserving the spectral fidelity, which also explains the visual color deviation of their results.

4.1.2. Cirrus correction over coastal areas

A cirrus image over a coastal area was simulated to validate the practicability of the proposed method for ocean surfaces, where the cirrus covers not only the ocean but also the land, as shown in Fig. 5a. The results of the three comparative methods are shown in Fig. 5b–d. The results of the proposed method, without and with the special treatment for the ocean area, are shown in Fig. 5e and f, respectively. Fig. 5g is the ground truth, which is mainly composed of ocean surface, mudflat, forest, and bare land. Visually, the performances of the different methods are similar to those in Fig. 4. The result of the ICARM method suffers from severe color distortion in the land and ocean surfaces and shows lower color saturation than the cloud-free reference image. The result of the ACRM method shows that the cirrus over the land surface can be removed substantially, but dense cirrus still remains over the ocean surface, as the highlighted rectangle in Fig. 5c shows. The result of the ECCM method indicates that the cirrus can be removed completely in the entire scene, but the corrected cloudy region is much darker than the original clear regions over both land and ocean surfaces. Fig. 5e and f are the same over the land surface, with all the cirrus cloud removed, but differ significantly over the ocean surface. Fig. 5e shows an evident boundary between the corrected region and the clear region on the ocean surface. This is because the linear relationship between coastal and blue bands is different over ocean and land surfaces, resulting in misestimation of γ and improper correction over the ocean surface. The result of the proposed method reveals good spatial continuity in Fig. 5f with the adjustment of over the ocean surface, proving the practicability of the proposed parameter determination approach for ocean surfaces.

The three metrics for Fig. 5 were calculated and are listed in Table 2. In most cases, the scores of the ICARM method in all the VNIR bands show a poor performance in both the cloudy area and the full scene, which confirms the previous qualitative assessment. The metric scores of the ACRM and ECCM methods are satisfactory because the required homogeneous surfaces exist in the data. Comparing the last columns of Table 2 suggests that the parameter determination strategy for ocean surfaces cannot only promote the visual effect, but also the quantitative scores of the results.

According to the qualitative and quantitative comparisons of the two representative experiments on simulated data, it can be concluded that

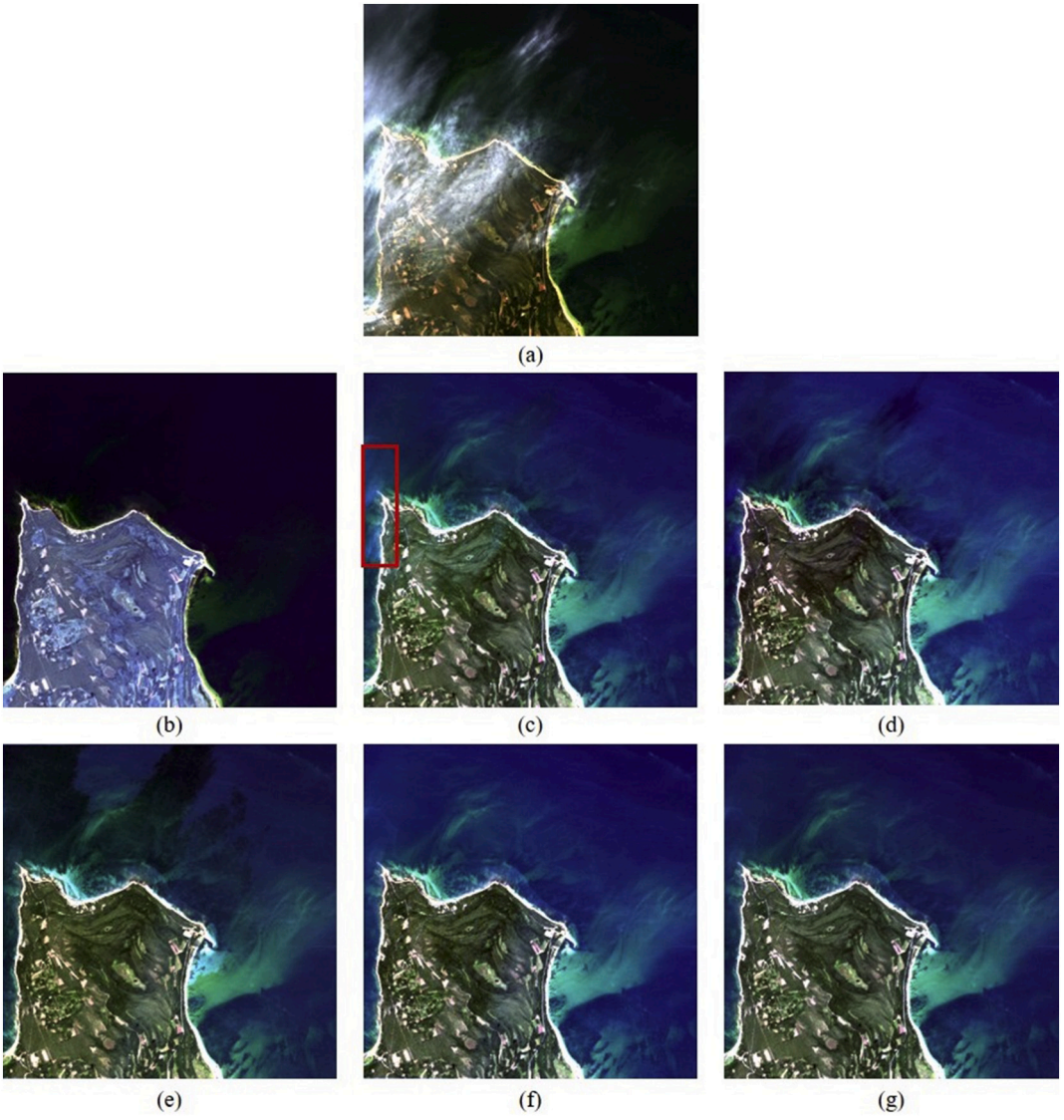

Fig. 5. Results for the simulated cirrus cloud image with a large area of ocean. (a) Simulated cirrus image. (b) ICARM. (c) ACRM. (d) ECCM. (e) Proposed method without the special treatment strategy. (f) Proposed method. (g) Ground truth.

Table 2
Quantitative assessment of the results of cirrus cloud correction over a coastal area.

			ICARM	ACRM	ECCM	Proposed*	Proposed
RMSE	Cloudy area	Band 1	4.9583	1.0916	1.6453	2.1000	0.6852
		Band 2	4.9583	0.6540	2.0777	2.0547	0.6758
		Band 3	3.4397	0.3527	0.9577	1.2096	0.4055
		Band 4	2.4589	0.1772	0.6478	0.7256	0.2476
		Band 5	3.3955	0.1039	0.3356	0.2535	0.0895
	Full scene	Band 1	4.4899	0.6669	1.0374	1.3434	0.3600
		Band 2	4.4900	0.4016	1.3069	1.2944	0.3394
		Band 3	3.1367	0.2148	0.6098	0.7576	0.2037
		Band 4	2.2812	0.1090	0.4080	0.4523	0.1244
		Band 5	3.0771	0.0636	0.2109	0.1569	0.0449
MAE	Cloudy area	Band 1	3.9932	3.2244	5.1224	4.9985	0.3527
		Band 2	3.9932	1.9234	5.9450	4.7697	0.3199
		Band 3	2.7633	0.7312	4.4095	2.7744	0.1868
		Band 4	1.9641	0.4935	1.9341	1.6438	0.1111
		Band 5	2.5902	0.3084	0.9601	0.5601	0.0381
	Full scene	Band 1	3.4586	0.4355	0.7083	0.8076	0.1864
		Band 2	3.4586	0.2673	0.7925	0.7666	0.1598
		Band 3	2.4154	0.1000	0.6291	0.4438	0.0935
		Band 4	1.7536	0.0699	0.2633	0.2619	0.0556
		Band 5	2.2792	0.0423	0.1233	0.0886	0.0191
SA	Cloudy area	/	2.7707	0.5745	0.9489	0.3898	0.1738
	Full scene	/	2.1187	0.3080	0.5046	0.2181	0.1226

Note: Proposed* means the result obtained using the proposed method without special treatment. Underline means that all the bands were used to calculate the metric value.

the proposed method can yield not only visually satisfactory results, but also high-fidelity spectral information for the VNIR bands, which will be beneficial for yielding quantitative products derived from the VNIR bands.

4.2. Analyses and results using acquired datasets

4.2.1. Cirrus correction over land areas

Three Landsat 8 OLI sub-images with various land covers were selected for the experiments, as shown in the first row of Fig. 6. The image in Fig. 6a is mainly covered with bare land; the primary land covers of the image in Fig. 6b are farmland, forest, and some urban areas; and the image in Fig. 6c is a typical forest scene. The second row shows the results of the ICARM method, in which problems with color distortion and under-correction exist because the cloud component is inaccurately estimated by ICA and the cirrus correlation in the VNIR bands is ignored. The third and fourth rows are the results of the ACRM and ECCM methods, where the cloudy regions are darkened and bluer after the correction, and are clearly different from the surroundings. This can be attributed to the inaccurate regression coefficients because of the insufficient homogeneous samples in the scenes. The results of the proposed method are presented in the last row. Clearly, all the cirrus cloud in these three scenes is removed, and the entire images are much more spatially coherent than the others, by visual assessment.

Fig. 7 shows a one-by-one comparison of the VNIR bands for Fig. 6a before and after correction using the proposed method. As the first row shows, all the VNIR bands are covered by cirrus cloud, and the intensities are evidently band-dependent, and decrease with the wavelength. After correction by the proposed method, the cirrus cloud in every VNIR band is removed, and the recovered information is very consistent with the original cloud-free regions, indicating that the spatial and spectral features are restored with high fidelity.

A cirrus cloud image and a paired clear image with a time interval of 16 days were selected to further evaluate the proposed method quantitatively, as exhibited in Fig. 8. Fig. 8a shows the cirrus-covered image centered at 147°9 ' 20.66 ' 'E, 27°9 ' 13.82 ' 'S acquired on May 1, 2018. The primary land cover is bare land. Fig. 8b is the cloud-free reference image acquired on April 15, 2018. Figs. 8c–8f are the results of the different methods. In general, all the methods can eliminate the cirrus cloud, but to different degrees and qualities. Fig. 8c shows that almost all the cirrus cloud is removed by the ICARM method, and the ground details are enhanced. However, compared with the reference image in Fig. 8b, the entire image is slightly more yellow and shows lower color saturation. In contrast, the ACRM and ECCM methods maintain the spectra of the clear regions better than the ICARM method, as can be observed in Fig. 8d and e. However, the corrected information in the cloudy region is quite different from the reference image, owing to the absence of homogeneous and dark surfaces in this scene, resulting in inaccurate estimation of the coefficients in these two methods. The corrected result obtained using the proposed algorithm is shown in Fig. 8f. A one-by-one comparison of Bands 1–5 before and after correction is exhibited in Fig. 9. Clearly, all the cirrus cloud is corrected completely in Bands 1–5, and the radiance of each VNIR band is spatially continuous and natural. Above all, with reference to the cloud-free image, the result of the proposed method in Fig. 8f is the closest to the ground truth, by visual assessment.

In addition to the RMSE, MAE, and SA, three other metrics, namely, the $\mathbf{R}^2$, the structural similarity index measure (SSIM), and correlation coefficient (CC), were also calculated to further evaluate the results. The closer the values of these three metrics get to 1, the better the result is. Table 3 shows the scores for all six metrics in both the cloudy area and the full scene. The performances of the ACRM and ECCM methods are similar, and the scores for the full scenes are better than those for the cloudy areas, owing to the good ability to maintain information in clear regions. The scores of the ICARM method in Bands 1–3 are close to those of the ACRM and ECCM methods, but it shows a better performance in Bands 4–5. These results indicate that the recovered information in Bands 4–5 more closely approaches the cloud-free reference image. Among the different methods, the metric values of the proposed method show the best performance in almost all the VNIR bands. The RMSE, MAE, and SA are the smallest, and the $\mathbf{R}^2$, SSIM, and CC are the closest to 1. These results indicate that the difference between the result of the

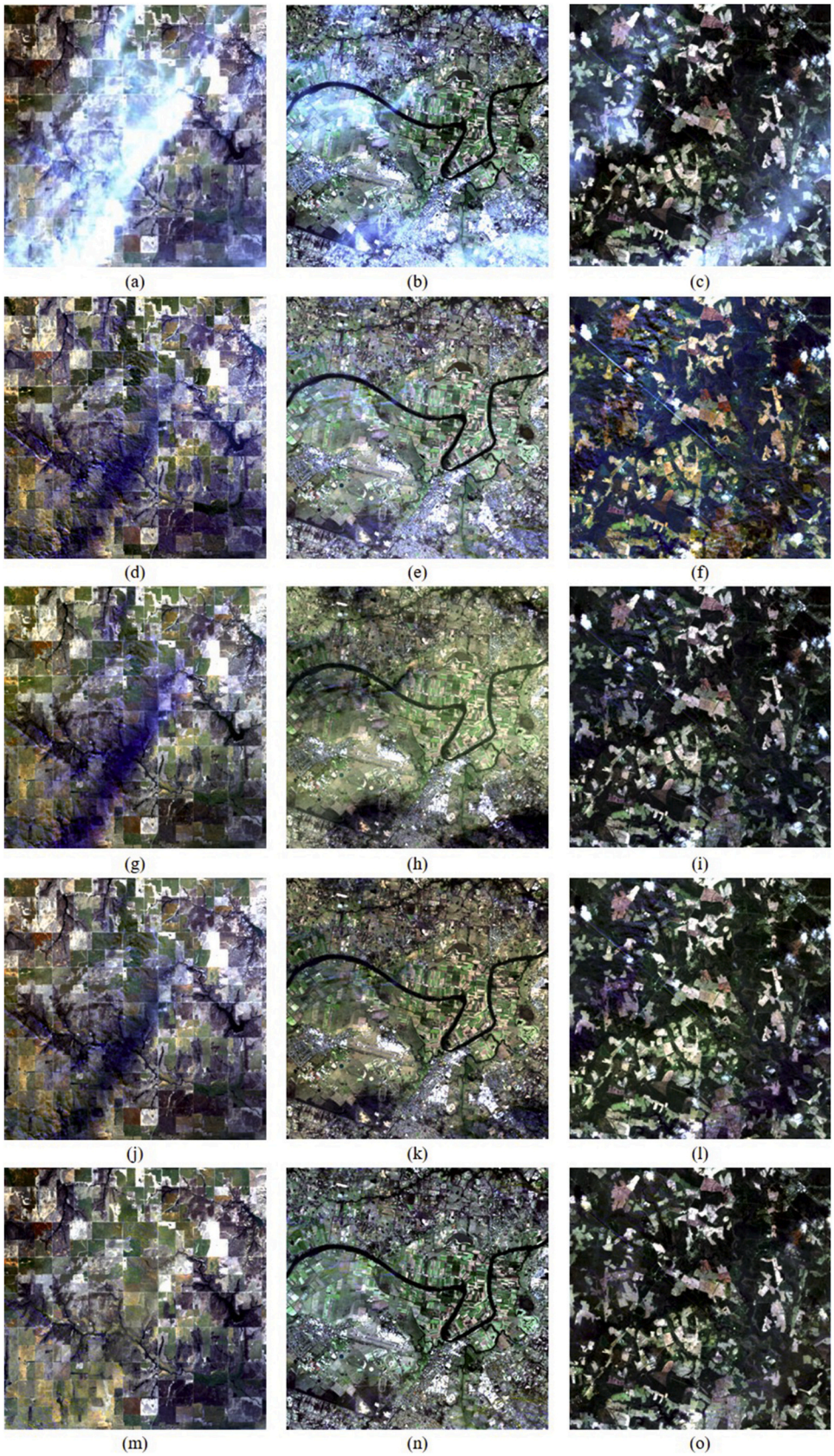

Fig. 6. Three acquired cirrus cloud images with complex land-cover types. The first row shows the three acquired cirrus cloud images with complex land-cover types. The second to fifth rows show the results of ICARM, ACRM, ECCM, and the proposed method.

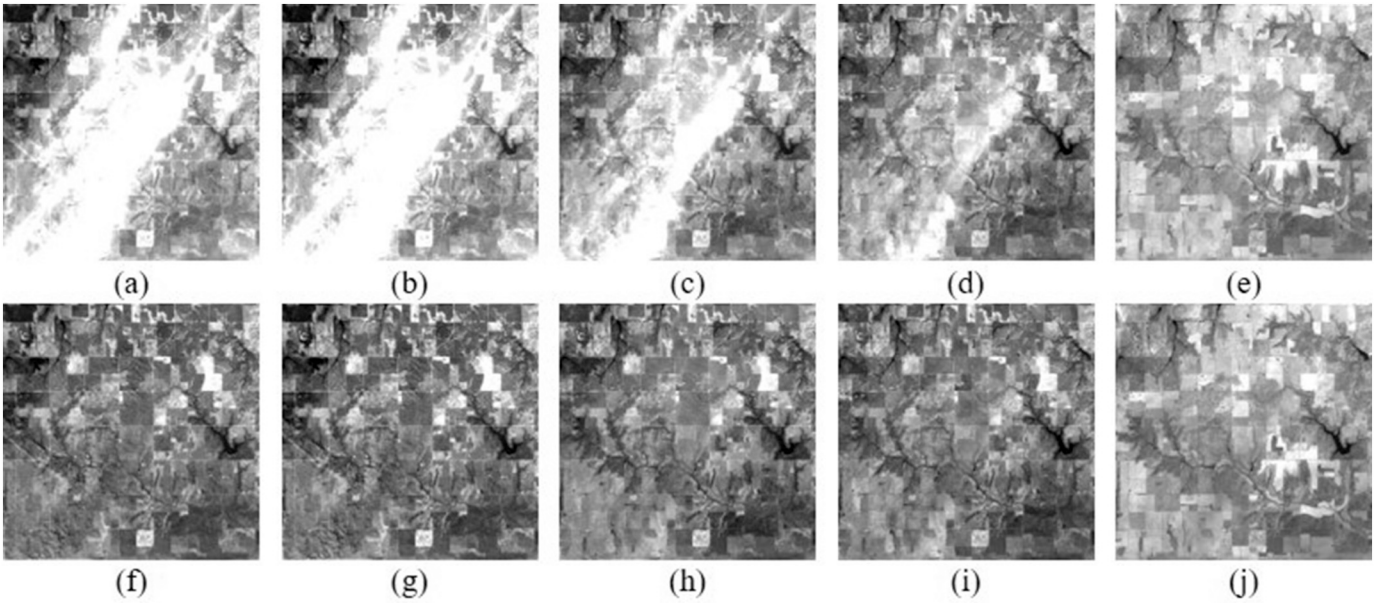

Fig. 7. Comparison of Bands 1–5 between the acquired cirrus cloud image and its correction results obtained using the proposed method. The first row, from left to right, shows the VNIR bands of the cirrus cloud image. The second row presents the corresponding results obtained using the proposed method.

proposed method and the reference image is the smallest, and the data consistency is the highest. Consequently, we can conclude that the proposed method shows a superior ability in recovering the ground information in VNIR images over land.

4.2.2. Cirrus correction over coastal areas

The results for cirrus cloud images with a large area of ocean surface are shown in Fig. 10. The image in Fig. 10a mainly consists of ocean surface, forest land, and grass land; the image in Fig. 10b mainly consists of ocean surface, farmland, and bare land; and the image in Fig. 10c mainly consists of ocean surface, grassland, and bare land. The results of the ICARM method suffer from spectral distortion, as before, and the saturation of clean regions is lower than that of the original images, as presented in the second row. The results of the ACRM and ECCM methods are displayed in the third and fourth rows, where the cirrus cloud over the ocean surface has been fully removed. However, color cast occurs in the land regions, as shown by the highlighted regions in Figs. 10h, i, k, and l, because both methods estimate the cirrus radiance of each band individually and ignore their relative correlations. The results of the proposed method are shown in the fifth row, where the cirrus cloud is removed completely, the spectral information of the clear region is maintained well, and the color of the entire scene is natural and coherent. These results indicate that the proposed method outperforms the compared methods in both cirrus correction and spectral restoration. However, a common problem with all the results is that artifacts are introduced, as shown by the red rectangle marked in Fig. 10g. This can be attributed to the difference of the parallax angles among the different bands, which means that the positions of the cirrus cloud in the different bands are not totally the same (Gao and Li, 2017). In the simulation experiments, as the positions of the cirrus cloud could be guaranteed to be the same in the different bands, no parallax error can be observed in the results.

Fig. 11 shows an individual comparison of the VNIR bands before and after correction by taking Fig. 10a as an example. The cirrus cloud in each VNIR band is totally removed, and the ground details are well restored. In addition, as the parallax angle problem exists in the OLI images, artifacts occur in the results shown in the second row.

To make a quantitative analysis, a cirrus-covered coastal OLI image centered at 115°41 ' 47.65 ' 'W and 28°8 ' 53.17 ' 'N and its paired cloud-free image were collected and are shown in Fig. 12, in which the image in Fig. 12a was acquired on March 12, 2018, and the image in Fig. 12b was acquired on March 28, 2018. The major land covers of this area are ocean surface and bare land. Fig. 12c–f are the results of the different methods. The ICARM, ACRM, and ECCM methods show similar performances, in that the that cirrus cloud over land surfaces is corrected, whereas residual cloud remains over the ocean surface, as exhibited in Fig. 12c–e. In contrast, in the result of the proposed method shown in Fig. 12f, the cirrus cloud over both land and ocean surfaces is removed completely, and the restored color characteristics are very close to those of the cloud-free reference image in Fig. 12b. The one-by-one comparison in Fig. 13 shows that all the VNIR bands are completely free from cirrus cloud, and the color of the original clear regions is maintained well. However, as with Fig. 11, several artifacts are introduced after the correction, due to the parallax error in the OLI images.

The six metrics for the different methods were calculated and are listed in Table 4, where it can be seen that the scores of the ICARM method are the worst, the scores of the ACRM and ECCM methods are very close, and the scores of the proposed method are the best, in most cases. The best scores for the VNIR bands indicate that the cirrus cloud is completely removed, while the lowest values of SA mean that the spectral information is accurately restored. The quantitative assessment is consistent with the visual assessment, suggesting that the proposed method is valid for cirrus correction in images covering a large area of ocean surface.

To further validate the effectiveness of the proposed method in cirrus correction over ocean surface, another experiment on an OLI coastal image with different land covers was carried out, as shown in Fig. 14. A band-by-band comparison is shown in Fig. 15. Fig. 14a shows the cloudy

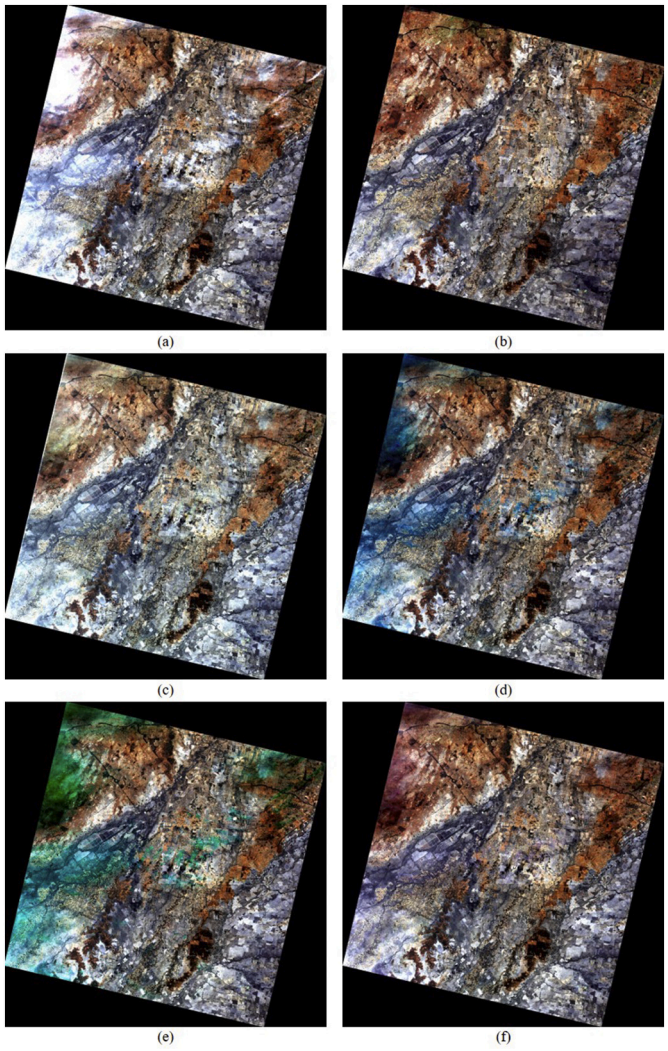

Fig. 8. Comparison of the different results obtained with the cloud-free reference image. (a) Original image with cirrus cloud on May 1, 2018. (b) Cloud-free image on April 15, 2018. (c) ICARM. (d) ACRM. (e) ECCM. (f) Proposed method.

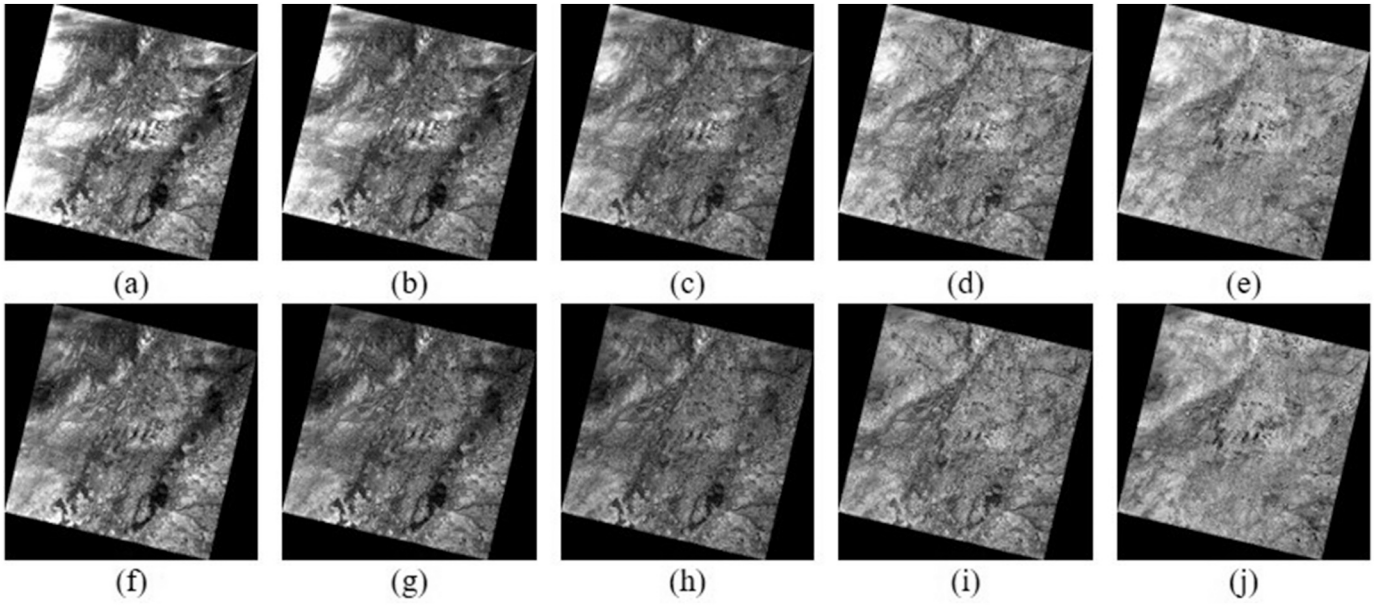

Fig. 9. Comparison of Bands 1–5 between the acquired cirrus cloud image and its correction results obtained using the proposed method. The first row, from left to right, shows the VNIR bands of the cirrus cloud image. The second row presents the corresponding results obtained using the proposed method.

image with cirrus cloud acquired on October 4, 2013, centered at 150°4 ' 52 ' 'E, 32°17 ' 48 ' 'S. The primary land covers are ocean surface, mudflat, wetland, farmland, and forest. Fig. 14b is the cloud-free reference image acquired on September 18, 2013. Fig. 14c–f present the results of the different methods. As shown in Fig. 14c, most of the cirrus cloud is removed, but some remains. Moreover, evident color distortion occurs in the areas with dense cirrus, as shown in the red rectangle. Similar to the ICARM method, the cirrus can be corrected by the ACRM method, but color shift can be seen in the results. In contrast, the cirrus over land and ocean surfaces is completely cleared by the ECCM method, but the color of the dense cirrus-covered areas is much darker than the reference image, suggesting that spectral distortion exists. For the proposed method, the cirrus in all the VNIR bands is removed, over both the land and ocean surfaces, as presented in Fig. 14f and Fig. 15, and the result is very close to the reference image in color. As in Figs. 12 and 13, artifacts again appear due to the parallax error of the OLI.

Table 5 lists the scores of the six metrics for the cloudy area and the full scene. Similar to Table 4, in almost all cases, the RMSE, MAE, and SA of the proposed method are the smallest, and the $\mathbf{R^2}$, SSIM, and CC are the closest to 1. The quantitative assessment indicates that the cirrus cloud in each VNIR band is cleared, and the surface information is restored accurately. The findings also prove that the parameter determination approach for ocean surfaces is effective and practical. Therefore, for cirrus-covered coastal images, the proposed method can achieve a satisfactory performance, in both the qualitative and quantitative aspects.

4.3. Applicability to MSI VNIR images of Sentinel-2

To further test the applicability of the proposed method to other sensors with similar bands, experiments on data captured by the Sentinel-2 MSI were carried out. Images with different locations, acquisition times, and land covers were selected over both land and coastal regions. The VNIR images were resampled to match the cirrus band because the spatial resolutions of the VNIR and cirrus bands of the Sentinel-2 MSI are different.

Fig. 16 shows the correction results obtained for a cirrus-covered MSI land image acquired on January 26, 2019, in which Fig. 16a is the original cirrus image, Fig. 16b is the cloud-free reference image acquired on January 31, 2019, and Fig. 16c is the corrected result. The primary land covers of the image are bare land and shrubs. The cirrus cloud over the different land covers is fully corrected, and the spectral and spatial details are well restored, showing high consistency with the cloud-free reference image.

The scores for the six metrics are listed in Table 6, with only the scores for the five VNIR bands with a similar central wavelength to Bands 1–5 of the OLI being shown here, i.e., Bands 1–4 and 8 of the MSI. The dynamic range of the radiance in the VNIR bands of Fig. 16a is from 6.3965 to 98.6812. Table 6 shows the values of the RMSE, MAE, and SA, which are small compared to the original radiance values, while the values of the $\mathbf{R^2}$, SSIM, and CC are between 0.9121 and 0.9664, i.e., very close to 1. These quantitative metrices suggest that the corrected result obtained for the MSI land image is satisfactory.

Fig. 17 shows the correction result for a coastal image captured by the Sentinel-2 MSI on January 18, 2019. Fig. 17a is the original image, where the cirrus cloud is scattered over both the land and ocean surfaces. The major land covers are ocean, bare land, and forest. Fig. 17b shows the cloud-free reference image acquired on January 23, 2019. Fig. 17c presents the correction result of the proposed method. Clearly, the cirrus cloud is totally corrected over the land and ocean surfaces, and the color is very close to that of the reference image.

Table 7 lists the scores of the six metrics for both the cloudy area and the full scene. The dynamic range of the radiance in the VNIR bands of Fig. 17a is from 2.4992 to 203.5013. The values of the RMSE and MAE are between 2.0966 and 2.9495 and 0.8732 to 1.4382, respectively. The values of the SA in the cloudy area and the full scene are 0.9711 and 0.8746, respectively. The values of the $\mathbf{R^2}$, SSIM, and CC vary between 0.9201 and 0.9978. These scores indicate that the proposed method is capable of achieving cirrus correction of Sentinel-2 MSI VNIR images covering different regions, and the results are qualitatively and quantitatively satisfactory.

Table 3
Quantitative assessment of the results of cirrus cloud correction over a land area.

			ICARM	ACRM	ECCM	Proposed
RMSE	Cloudy area	Band 1	3.6062	3.0875	3.3421	2.2200
		Band 2	3.9487	3.5465	4.0894	2.8932
		Band 3	4.2113	4.5373	4.0654	3.8948
		Band 4	5.0897	11.4361	18.9340	4.7632
		Band 5	6.1226	15.0489	14.3030	5.8818
	Full scene	Band 1	2.9827	2.8560	2.9858	2.1027
		Band 2	3.5702	3.4735	3.7439	2.7781
		Band 3	4.2392	4.3470	4.1856	3.6813
		Band 4	5.0365	8.2596	12.8192	4.4604
		Band 5	5.3186	10.3171	9.8965	4.8037
MAE	Cloudy area	Band 1	2.5070	2.1916	2.3025	1.2271
		Band 2	2.7765	2.5139	2.8194	1.6203
		Band 3	3.0372	3.2303	2.9160	2.3624
		Band 4	3.9563	8.2930	13.9513	3.0622
		Band 5	4.7907	11.1748	10.6594	3.9400
	Full scene	Band 1	2.0647	1.9146	1.9744	1.1928
		Band 2	2.8629	2.3204	2.4687	1.6304
		Band 3	2.9527	2.9316	2.8158	2.2571
		Band 4	3.8759	5.3283	7.7353	2.8101
		Band 5	3.8690	6.3379	6.1370	2.9449
SA	Cloudy area	/	2.8238	5.9891	7.5202	2.2730
	Full scene	/	2.2224	3.3018	3.9477	1.7489
$\mathbf{R^2}$	Cloudy area	Band 1	0.7457	0.7982	0.7809	0.8592
		Band 2	0.7855	0.8232	0.7999	0.8770
		Band 3	0.8033	0.8021	0.8160	0.8503
		Band 4	0.7973	0.5202	0.2683	0.8931
		Band 5	0.6313	0.2354	0.2591	0.8125
	Full scene	Band 1	0.7730	0.8003	0.7807	0.8822
		Band 2	0.7899	0.8111	0.7847	0.8942
		Band 3	0.7777	0.7765	0.7880	0.8745
		Band 4	0.7903	0.5756	0.3170	0.8787
		Band 5	0.6509	0.2722	0.2933	0.8059
SSIM	Cloudy area	Band 1	0.9183	0.9358	0.9299	0.9565
		Band 2	0.9185	0.9336	0.9245	0.9326
		Band 3	0.9192	0.9194	0.9253	0.9380
		Band 4	0.8782	0.7645	0.5449	0.9201
		Band 5	0.8153	0.5657	0.5935	0.8621
	Full scene	Band 1	0.9332	0.9402	0.9342	0.9614
		Band 2	0.9259	0.9327	0.9228	0.9518
		Band 3	0.9141	0.9126	0.9175	0.9310
		Band 4	0.8701	0.8039	0.6220	0.9277
		Band 5	0.8230	0.6317	0.6513	0.8664
CC	Cloudy area	Band 1	0.8636	0.8934	0.8837	0.8944
		Band 2	0.8863	0.9073	0.8944	0.9058
		Band 3	0.8963	0.8956	0.9033	0.8937
		Band 4	0.8029	0.7213	0.5180	0.8820
		Band 5	0.7945	0.4852	0.5090	0.8743
	Full scene	Band 1	0.8792	0.8946	0.8836	0.9162
		Band 2	0.8888	0.9006	0.8858	0.9191
		Band 3	0.8819	0.8812	0.8877	0.8989
		Band 4	0.8190	0.7587	0.5631	0.8873
		Band 5	0.8068	0.5217	0.5415	0.8973

Note: Underline means that all the bands were used to calculate the metric value.

5. Discussion

The experiments undertaken in this study on Landsat 8 OLI and Sentinel-2 MSI VNIR data verified the cirrus correction ability of the proposed method. However, two problems still need to be discussed. One is the applicability of the proposed method to more sensors with similar bands. The other is whether the proposed method works when there is ground information mixed in the cirrus band.

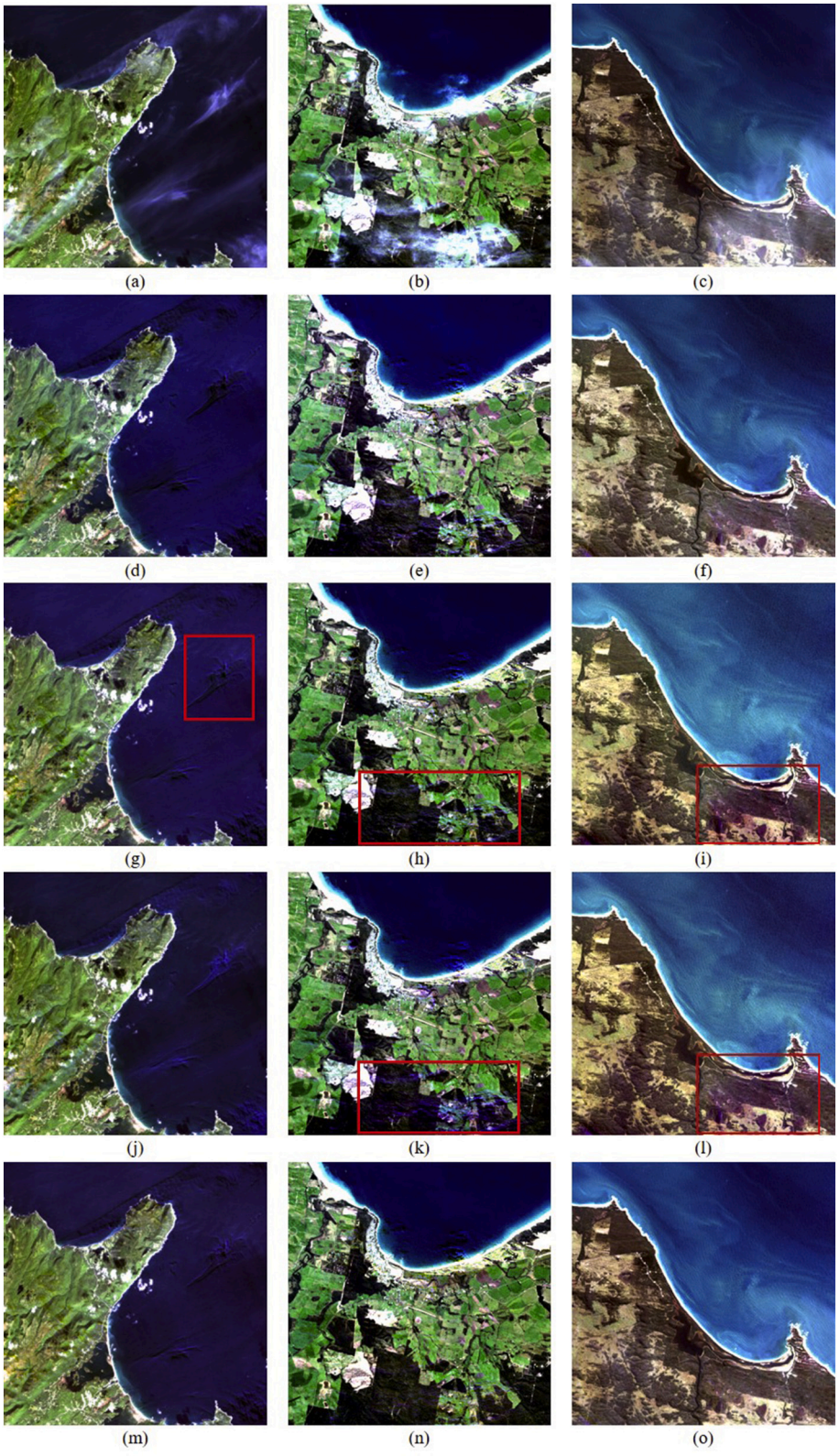

Fig. 10. Three acquired cirrus cloud images over a coastal area. The first row exhibits the three acquired cirrus cloud images over the coastal area. The second to fifth rows show the results of ICARM, ACRM, ECCM, and the proposed method.

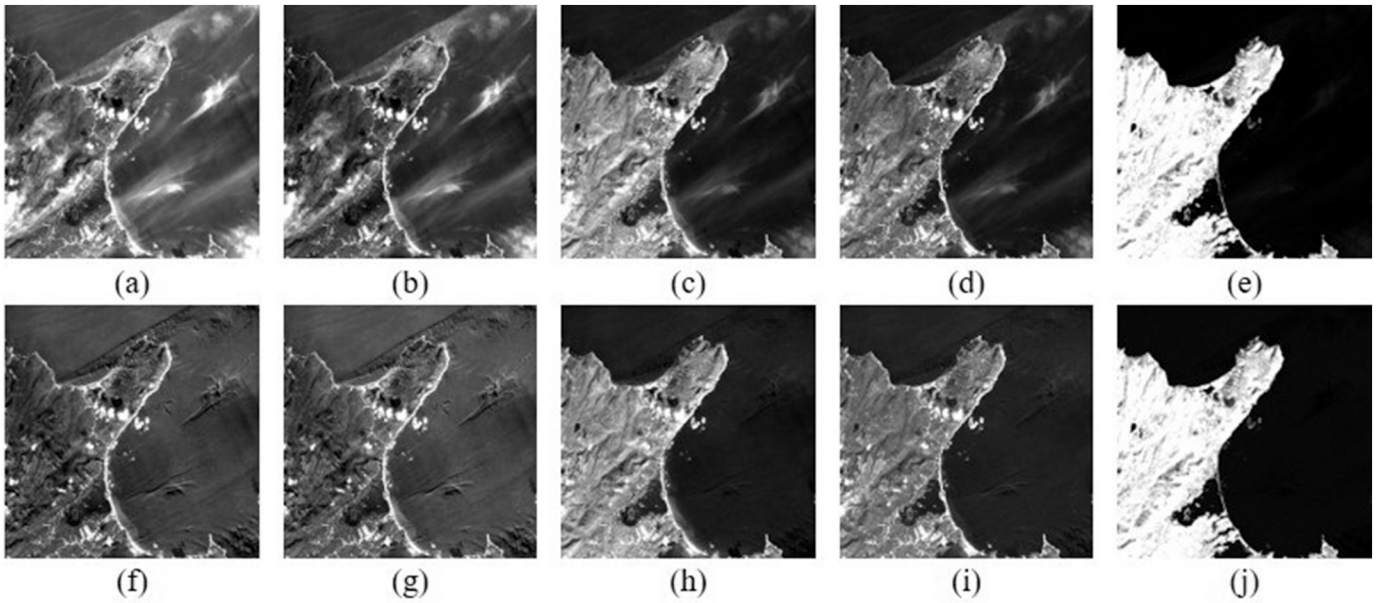

Fig. 11. Comparison of Bands 1–5 between the acquired cirrus cloud image and its correction results obtained using the proposed method. The first row, from left to right, shows the VNIR bands of the cirrus cloud image. The second row presents the corresponding results obtained using the proposed method.

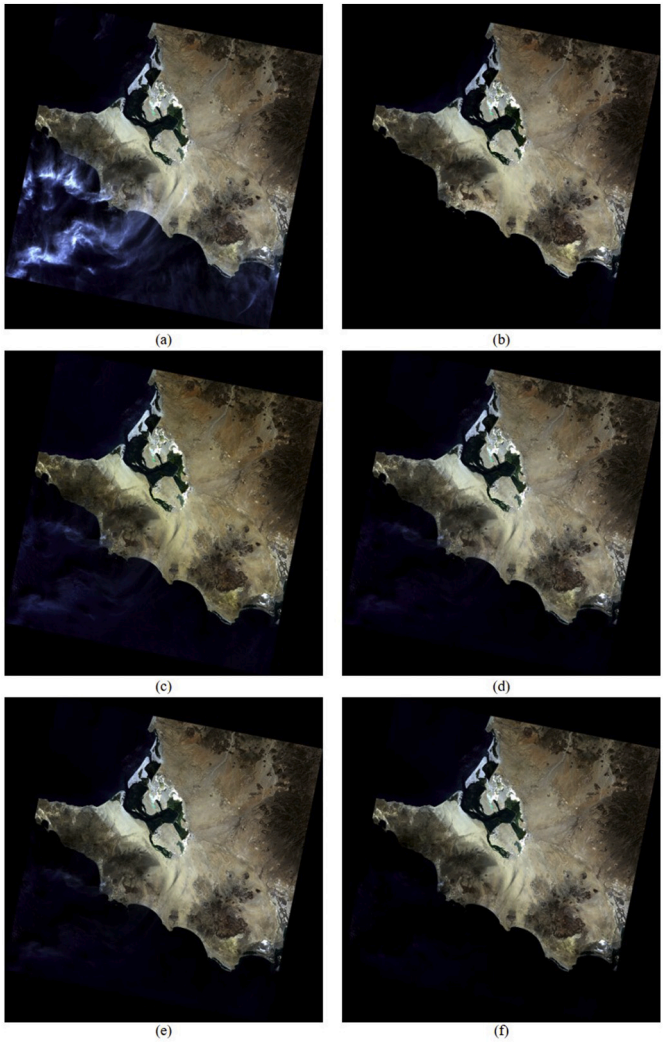

Fig. 12. Comparison of the different results obtained with the cloud-free reference image. (a) Original image with cirrus cloud on March 12, 2018. (b) Cloud-free image on March 28, 2018. (c) ICARM. (d) ACRM. (e) ECCM. (f) Proposed method.

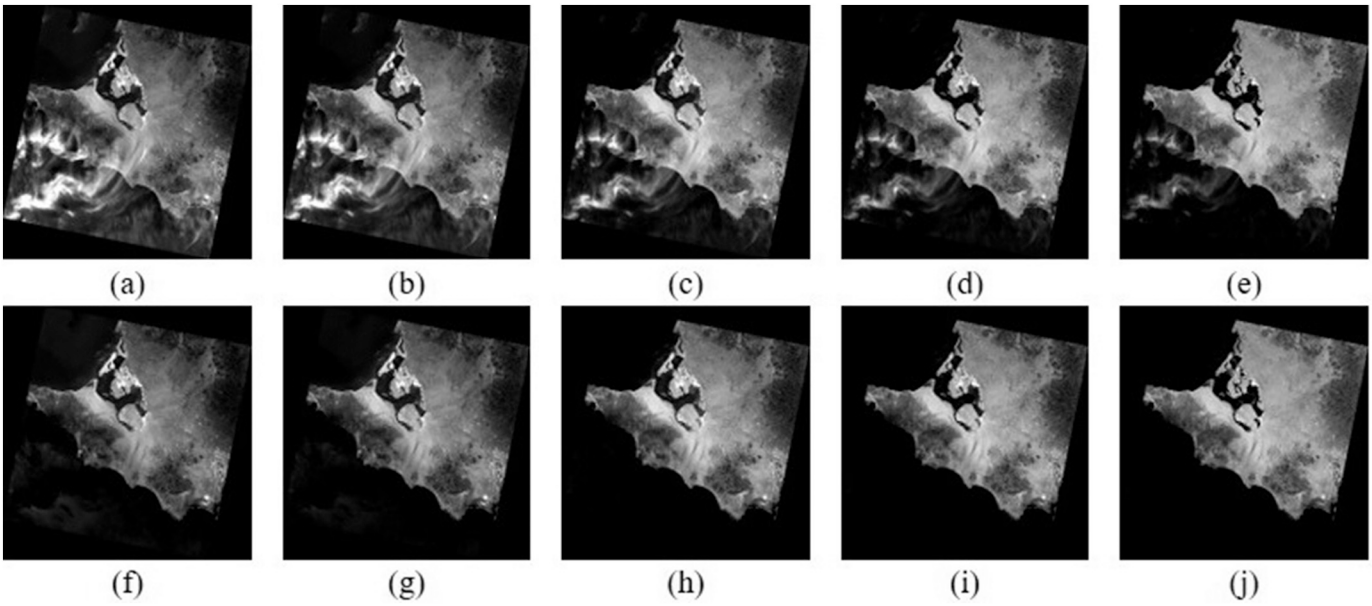

Fig. 13. Comparison of Bands 1–5 between the acquired cirrus cloud image and its correction results obtained using the proposed method. The first row, from left to right, shows the VNIR bands of the cirrus cloud image. The second row presents the corresponding results obtained using the proposed method.

Table 4
Quantitative assessment of the results of cirrus cloud correction over a coastal area.

			ICARM	ACRM	ECCM	Proposed
RMSE	Cloudy area	Band 1	14.0369	8.3890	7.4747	6.8670
		Band 2	13.8571	9.0883	8.4823	7.8672
		Band 3	11.0339	9.6815	9.0344	8.0164
		Band 4	10.3315	9.6699	9.2415	8.2664
		Band 5	7.0790	7.0715	6.7647	5.9299
	Full scene	Band 1	11.4398	6.3464	5.7885	5.2349
		Band 2	11.3840	6.9603	6.6063	6.0497
		Band 3	9.0787	7.3293	6.9455	6.1249
		Band 4	8.4532	7.3443	7.1300	6.3283
		Band 5	5.8497	5.4764	5.3420	4.5507
MAE	Cloudy area	Band 1	11.0188	5.8821	5.6461	5.3687
		Band 2	10.7242	6.3137	6.3405	6.0612
		Band 3	8.5479	6.4388	6.5947	5.9478
		Band 4	7.8623	6.1225	6.5703	5.9508
		Band 5	5.0939	4.2900	4.5754	3.9906
	Full scene	Band 1	8.0481	3.7526	3.6446	3.1638
		Band 2	7.7889	4.1034	4.1257	3.6450
		Band 3	6.0981	4.2186	4.3167	3.6615
		Band 4	5.5715	4.1851	4.4322	3.7865
		Band 5	3.5351	2.9313	3.0878	2.4689
SA	Cloudy area	/	2.9939	2.8438	3.0321	2.1467
	Full scene	/	1.9808	1.7937	1.8848	1.0961
R^2	Cloudy area	Band 1	0.5882	0.8220	0.8580	0.9098
		Band 2	0.7709	0.8835	0.9036	0.9227
		Band 3	0.9334	0.9436	0.9542	0.9696
		Band 4	0.9565	0.9589	0.9649	0.9806
		Band 5	0.9667	0.9659	0.9695	0.9858
	Full scene	Band 1	0.7762	0.9163	0.9275	0.9653
		Band 2	0.8609	0.9400	0.9455	0.9751
		Band 3	0.9509	0.9663	0.9702	0.9877
		Band 4	0.9678	0.9746	0.9768	0.9909
		Band 5	0.9754	0.9780	0.9794	0.9941
SSIM	Cloudy area	Band 1	0.7608	0.9119	0.9174	0.9222
		Band 2	0.8547	0.9381	0.9374	0.9436
		Band 3	0.9474	0.9642	0.9644	0.9751
		Band 4	0.9642	0.9707	0.9722	0.9826
		Band 5	0.9735	0.9730	0.9766	0.9869
	Full scene	Band 1	0.8856	0.9597	0.9629	0.9705
		Band 2	0.9274	0.9704	0.9707	0.9790

(*continued on next page*)

Table 4 (*continued*)

			ICARM	ACRM	ECCM	Proposed
		Band 3	0.9730	0.9827	0.9830	0.9872
		Band 4	0.9820	0.9867	0.9867	0.9887
		Band 5	0.9866	0.9885	0.9885	0.9895
CC	Cloudy area	Band 1	0.7669	0.9067	0.9263	0.9323
		Band 2	0.8780	0.9399	0.9506	0.9580
		Band 3	0.9661	0.9714	0.9768	0.9870
		Band 4	0.9780	0.9792	0.9823	0.9923
		Band 5	0.9832	0.9828	0.9846	0.9946
	Full scene	Band 1	0.8810	0.9572	0.9631	0.9712
		Band 2	0.9278	0.9695	0.9724	0.9810
		Band 3	0.9752	0.9830	0.9850	0.9950
		Band 4	0.9838	0.9872	0.9883	0.9982
		Band 5	0.9876	0.9889	0.9896	0.9995

Note: Underline means that all the bands were used to calculate the metric value.

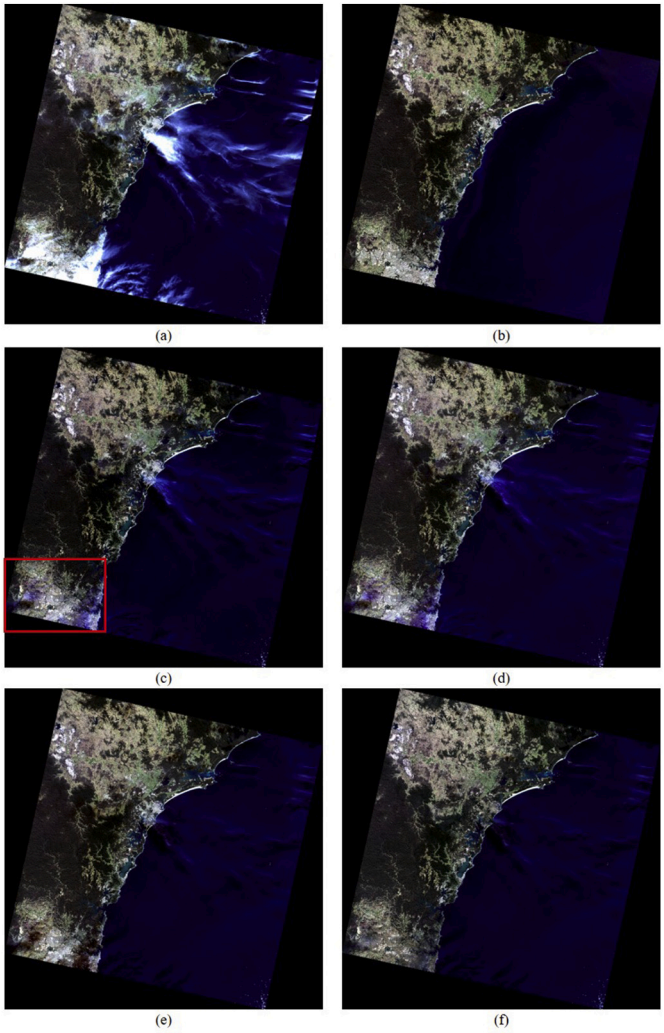

Fig. 14. Comparison of the different results obtained with the cloud-free reference image. (a) Original image with cirrus cloud on October 4, 2013. (b) Cloud-free image on September 18, 2013. (c) ICARM. (d) ACRM. (e) ECCM. (f) Proposed method.

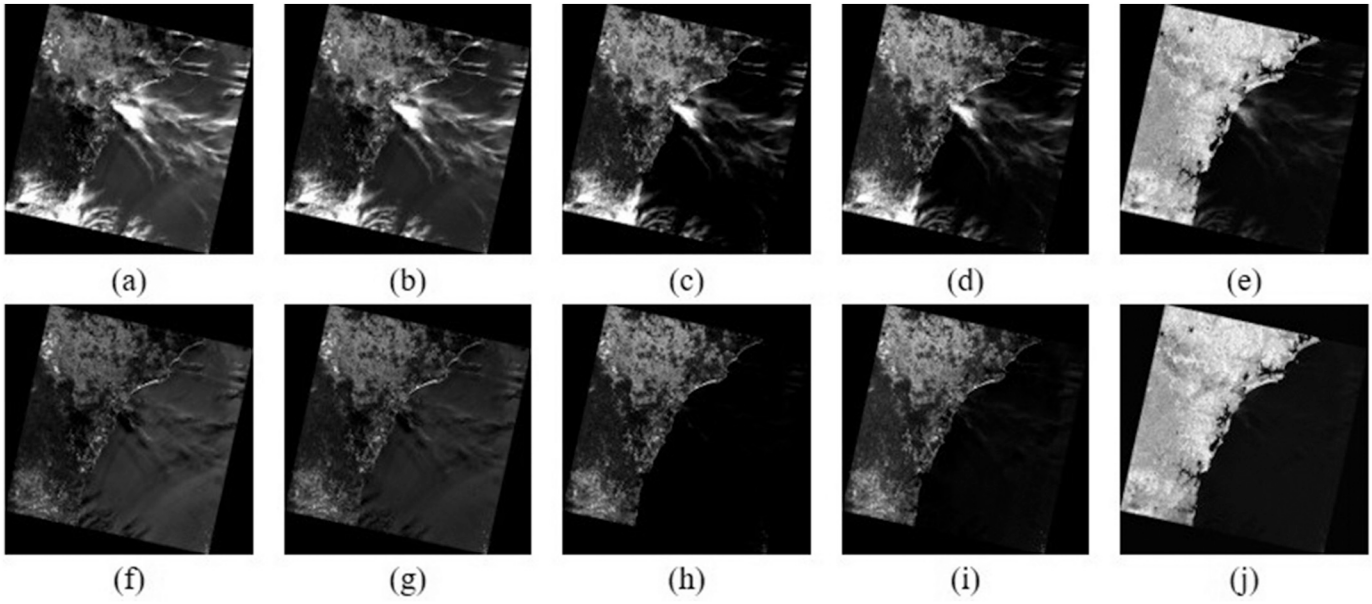

Fig. 15. Comparison of Bands 1–5 between the acquired cirrus cloud image and its correction results obtained using the proposed method. The first row, from left to right, shows the VNIR bands of the cirrus cloud image, and the second row presents the corresponding results obtained using the proposed method.

5.1. Applicability to other sensors

To further investigate the proposed method's applicability to other sensors with similar bands, six cirrus cloud images were further collected from the Terra MODIS satellite, the AVIRIS instrument, and the Earth Orbiter-1 (EO-1) Hyperion instrument for testing. The results are evaluated both qualitatively and quantitatively. Visually, all the cirrus clouds in the VNIR bands of the data are corrected completely, without color distortion, and the results are very close to the cloud-free reference images. Quantitatively, the values of the RMSE, MAE, and SA are less than 3.00, 2.03, and 0.87, respectively, and the values of the $\mathbf{R^2}$, SSIM, and CC are greater than 0.90. Therefore, it can be concluded that when the required bands are available, the proposed method can be used for cirrus correction in VNIR images, and visually and quantitatively satisfactory results can be obtained.

5.2. Ground pixels in the cirrus band

Within the spectral range of Band 9 (1.363–1.384 μm), the water vapor or moisture in the atmosphere absorbs nearly all the upward radiation containing the ground surface information. Thus, cirrus cloud can be detected by Band 9 when there is abundant water vapor or moisture between the observed ground target and the sensor. When the water vapor or moisture in the atmosphere is relatively low, the ground reflectance in the 1.363–1.384 μm range cannot be completely absorbed, thereby causing the occurrence of ground targets in Band 9 and affecting the correction results. In the results, the mixed ground pixels would be identified as cirrus cloud pixels and wrongly corrected, while the correction of the true cloudy pixels would not be affected. If the mixed ground pixels could be screened by a certain criteria, the possible errors could be avoided. We will further investigate a screening method in our future work.

6. Conclusions

In this paper, a cirrus cloud correction method based on a scattering law has been proposed to restore the ground information clearly and accurately for the VNIR images of the Landsat 8 OLI. Both simulated and acquired datasets were generated and collected to perform the experiments, and qualitative and quantitative assessments were conducted to evaluate the effects of the proposed method. Qualitatively, the cirrus cloud in the VNIR images could be effectively removed for both land and ocean surfaces, owing to the reasonable estimation of the cirrus radiance in each individual band. The color of the corrected cloudy regions was consistent with the clear regions because of the accurate spectral restoration based on the scattering law. Quantitatively, in the experiments with simulated images, the RMSE, MAE, and SA values of the proposed method were better than those of the compared methods, over both land and ocean surfaces. In the experiments with acquired images, six metrics were calculated by referencing the temporally adjacent cloud-free images, and the results showed that the proposed method was superior to the compared methods. In addition, the proposed method's applicability for different sensors with similar bands was also validated, including Sentinel-2 MSI, Terra MODIS, AVIRIS, and EO-1 Hyperion. However, it should be noted that the proposed method should be carefully used when ground targets exist in the cirrus band. In summary, the proposed method is effective for cirrus correction in VNIR images of various scenes, and the corrected results have high spatial and spectral fidelity.

CRediT authorship contribution statement

Chi Zhang: Conceptualization, Methodology, Software, Data curation, Writing - original draft, Writing - review & editing. **Huifang Li:** Conceptualization, Supervision, Validation, Funding acquisition, Writing - review & editing. **Huanfeng Shen:** Supervision, Validation, Funding acquisition, Writing - review & editing.

Declaration of competing interest

The authors declare that they have no known competing financial interests or personal relationships that could have appeared to influence the work reported in this paper.

Table 5
Quantitative assessment of the results of cirrus cloud correction over a coastal area.

			ICARM	ACRM	ECCM	Proposed
RMSE	Cloudy area	Band 1	3.6133	5.9689	3.9710	3.2675
		Band 2	4.2895	3.8711	4.3247	3.8396
		Band 3	3.9834	4.0743	4.5219	3.4053
		Band 4	4.4101	4.1623	4.5246	3.4539
		Band 5	5.8203	5.7161	5.5452	3.9346
	Full scene	Band 1	3.5282	4.2735	3.0821	3.0125
		Band 2	3.3903	3.0877	3.3703	3.1895
		Band 3	3.4738	3.1918	3.5015	3.2626
		Band 4	3.4131	3.2615	3.4852	3.2172
		Band 5	4.2256	4.4445	4.2607	3.2034
MAE	Cloudy area	Band 1	2.4385	2.9473	2.0609	1.5145
		Band 2	2.7814	2.2938	2.1952	1.7237
		Band 3	2.1368	2.0192	2.0789	1.7130
		Band 4	2.1711	2.0507	2.0491	1.6867
		Band 5	2.8266	2.9268	2.8547	1.9641
	Full scene	Band 1	1.5662	1.9535	1.5434	0.8905
		Band 2	1.7443	1.7070	1.6514	1.0434
		Band 3	1.6082	1.5559	1.5882	1.0328
		Band 4	1.6424	1.5722	1.5652	1.0112
		Band 5	2.2082	2.2230	2.1608	1.3517
SA	Cloudy area	/	2.0544	2.7891	1.8514	1.5611
	Full scene	/	1.6868	2.0535	1.5882	1.1988
$\mathbf{R^2}$	Cloudy area	Band 1	0.5920	0.8350	0.8176	0.8704
		Band 2	0.6811	0.8580	0.8265	0.9091
		Band 3	0.8699	0.8883	0.8581	0.9693
		Band 4	0.8859	0.9024	0.8809	0.9767
		Band 5	0.9640	0.9612	0.9629	0.9944
	Full scene	Band 1	0.7392	0.8401	0.8432	0.8922
		Band 2	0.7953	0.8756	0.8556	0.9257
		Band 3	0.9149	0.9019	0.8827	0.9748
		Band 4	0.9194	0.9134	0.9025	0.9806
		Band 5	0.9752	0.9724	0.9744	0.9959
SSIM	Cloudy area	Band 1	0.8616	0.7663	0.8688	0.8864
		Band 2	0.8720	0.9097	0.8820	0.8914
		Band 3	0.9195	0.9426	0.9311	0.9472
		Band 4	0.9230	0.9468	0.9380	0.9508
		Band 5	0.9402	0.9775	0.9788	0.9811
	Full scene	Band 1	0.9090	0.8438	0.9101	0.9256
		Band 2	0.9075	0.9299	0.9157	0.9330
		Band 3	0.9127	0.9567	0.9491	0.9427
		Band 4	0.9217	0.9595	0.9547	0.9520
		Band 5	0.9469	0.9854	0.9866	0.9870
CC	Cloudy area	Band 1	0.7694	0.5788	0.7467	0.8607
		Band 2	0.8253	0.8706	0.8225	0.8983
		Band 3	0.9127	0.9425	0.9263	0.9383
		Band 4	0.9212	0.9500	0.9386	0.9417
		Band 5	0.9818	0.9804	0.9813	0.9834
	Full scene	Band 1	0.8598	0.6634	0.8020	0.8715
		Band 2	0.8718	0.8807	0.8577	0.9010
		Band 3	0.9365	0.9497	0.9395	0.9429
		Band 4	0.9288	0.9557	0.9500	0.9381
		Band 5	0.9575	0.9861	0.9871	0.9876

Note: Underline means that all the bands were used to calculate the metric value.

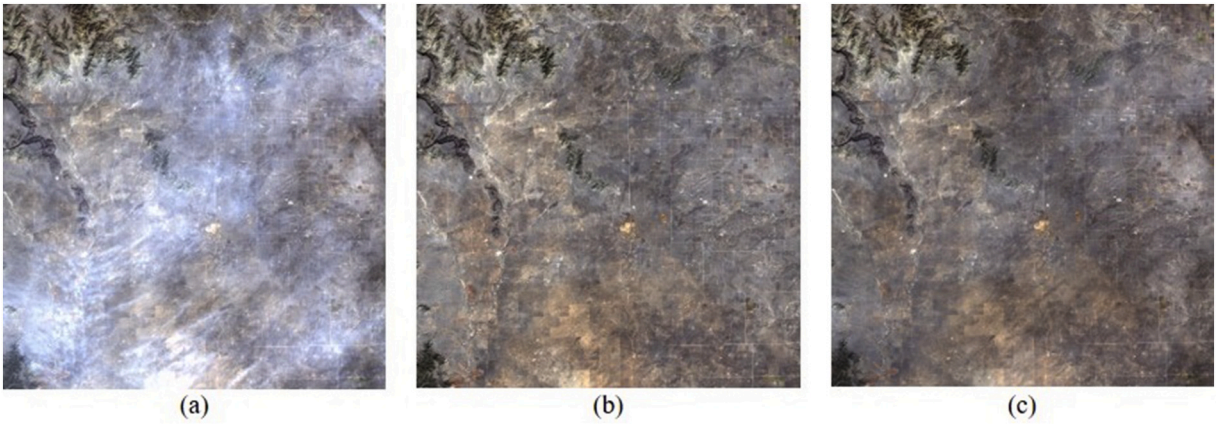

Fig. 16. Cirrus correction results for a Sentinel-2 MSI image over a land area obtained using the proposed method. (a) Original image with cirrus acquired on January 26, 2019. (b) Cloud-free reference image captured on January 31, 2019. (c) Corrected image.

Table 6
Quantitative assessment for the different VNIR bands of the Sentinel-2 MSI.

		Band 1	Band 2	Band 3	Band 4	Band 8
RMSE	Cloudy area	0.3798	0.6389	0.9700	1.2228	1.2763
	Full scene	0.3531	0.6072	0.9421	1.1819	1.2795
MAE	Cloudy area	0.2387	0.5445	0.8414	0.9247	0.9441
	Full scene	0.2051	0.4973	0.7843	0.8422	0.8756
SA	Cloudy area	0.7786				
	Full scene	0.7281				
R^2	Cloudy area	0.9459	0.9664	0.9627	0.9121	0.9347
	Full scene	0.9368	0.9473	0.9457	0.9211	0.9518
SSIM	Cloudy area	0.9544	0.9432	0.9411	0.9331	0.9376
	Full scene	0.9559	0.9450	0.9420	0.9338	0.9386
CC	Cloudy area	0.9247	0.9434	0.9416	0.9456	0.9570
	Full scene	0.9128	0.9337	0.9443	0.9466	0.9618

Note: Underline means that all the bands were used to calculate the metric value.

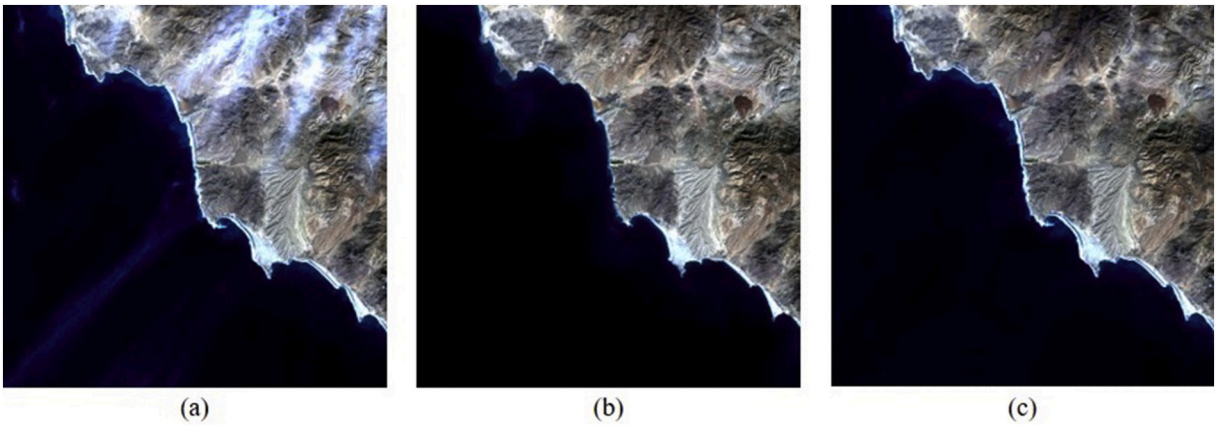

Fig. 17. Cirrus correction results for a Sentine l-2 MSI image over a coastal area obtained using the proposed method. (a) Original image with cirrus acquired on January 18, 2019. (b) Cloud-free reference image acquired on January 23, 2019. (c) Corrected image.

Table 7
Quantitative assessment of the different VNIR bands of a Sentinel-2 MSI image over a coastal area.

		Band 1	Band 2	Band 3	Band 4	Band 8
RMSE	Cloudy area	2.2888	2.9495	2.6078	2.4880	2.7543
	Full scene	2.4035	2.2065	2.7434	2.3928	2.0966
MAE	Cloudy area	0.8732	0.9025	1.0926	1.3264	1.4382
	Full scene	1.1182	1.1436	1.1574	1.2492	1.2341
SA	Cloudy area	0.9711				
	Full scene	0.8746				
R^2	Cloudy area	0.9417	0.9633	0.9830	0.9911	0.9906
	Full scene	0.9595	0.9742	0.9895	0.9966	0.9978
SSIM	Cloudy area	0.9335	0.9114	0.9497	0.9311	0.9621
	Full scene	0.9372	0.9299	0.9498	0.9329	0.9708
CC	Cloudy area	0.9314	0.9201	0.9418	0.9246	0.9627
	Full scene	0.9361	0.9254	0.9452	0.9259	0.9688

Note: Underline means that all the bands were used to calculate the metric value.

Acknowledgments

This work was funded by the National Natural Science Foundation of China (grants 41871246 and 41631180).

References

Bucholtz, A., 1995. Rayleigh-scattering calculations for the terrestrial atmosphere. Appl. Opt. 34, 2765–2773.
Chanda, B., Majumder, D.D., 1991. An iterative algorithm for removing the effect of thin cloud cover from Landsat imagery. Math. Geol. 23, 853–860.
Chavez Jr., P.S., 1988. An improved dark-object subtraction technique for atmospheric scattering correction of multispectral data. Remote Sens. Environ. 24, 459–479.
Chavez Jr., P.S., 1989. Radiometric calibration of Landsat Thematic Mapper multispectral images. Photogramm. Eng. Remote. Sens. 55, 1285–1294.
Chen, S., Chen, X., Chen, J., Jia, P., Cao, X., Liu, C., 2016. An iterative haze optimized transformation for automatic cloud/haze detection of Landsat imagery. IEEE Trans. Geosci. Remote Sens. 54, 2682–2694.
Chepfer, H., Goloub, P., Spinhirne, J., Flamant, P.H., Lavorato, M., Sauvage, L., Brogniez, G., Pelon, J., 2000. Cirrus cloud properties derived from POLDER-1/ADEOS polarized radiances: first validation using a ground-based lidar network. J. Appl. Meteorol. 39, 154–168.
Crist, E.P., Cicone, R.C., 1984. A physically-based transformation of Thematic Mapper data – the TM Tasseled Cap. IEEE Trans. Geosci. Remote Sens. 256–263.
Dessler, A., Yang, P., 2003. The distribution of tropical thin cirrus clouds inferred from Terra MODIS data. J. Clim. 16, 1241–1247.
Drusch, M., Del Bello, U., Carlier, S., Colin, O., Fernandez, V., Gascon, F., Hoersch, B., Isola, C., Laberinti, P., Martimort, P., 2012. Sentinel-2: ESA's optical high-resolution mission for GMES operational services. Remote Sens. Environ. 120, 25–36.
Du, Y., Guindon, B., Cihlar, J., 2002. Haze detection and removal in high resolution satellite image with wavelet analysis. IEEE Trans. Geosci. Remote Sens. 40, 210–217.
Gao, B.C., Li, R.R., 2000. Quantitative improvement in the estimates of NDVI values from remotely sensed data by correcting thin cirrus scattering effects. Remote Sens. Environ. 74, 494–502.
Gao, B.C., Li, R.R., 2012. Removal of thin cirrus scattering effects for remote sensing of ocean color from space. IEEE Geosci. Remote Sens. Lett. 5, 972–976.
Gao, B.C., Li, R.R., 2017. Removal of thin cirrus scattering effects in Landsat 8 OLI images using the cirrus detecting channel. Remote Sens. 9, 834.
Gao, B.C., Kaufman, Y.J., Han, W., Wiscombe, W.J., 1998. Correction of thin cirrus path radiances in the 0.4–1.0 μm spectral region using the sensitive 1.375 μm cirrus detecting channel. J. Geophys. Res. Atmos. 103, 32169–32176.
Gao, B.C., Yang, P., Han, W., Li, R.-R., Wiscombe, W.J., 2002. An algorithm using visible and 1.38−/spl mu/m channels to retrieve cirrus cloud reflectances from aircraft and satellite data. IEEE Trans. Geosci. Remote Sens. 40, 1659–1668.
He, X.Y., Hu, J.B., Chen, W., Li, X.Y., 2010. Haze removal based on advanced haze-optimized transformation (AHOT) for multispectral imagery. Int. J. Remote Sens. 31, 5331–5348.
Li, H., Zhang, L., Shen, H., Li, P., 2012. A variational gradient-based fusion method for visible and SWIR imagery. Photogramm. Eng. Remote. Sens. 78, 947–958.
Liu, J., Wang, X., Chen, M., Liu, S., Zhou, X., Shao, Z., Liu, P., 2014. Thin cloud removal from single satellite images. Opt. Express 22, 618–632.
Loyd, C., 2013. Putting Landsat 8's Bands to Work. NASA, USA.

Lucke, R.L., Corson, M., McGlothlin, N.R., Butcher, S.D., Wood, D.L., Korwan, D.R., Chen, D.T., 2011. Hyperspectral Imager for the Coastal Ocean: instrument description and first images. Appl. Opt. 11, 1501–1516.
Lv, H., Wang, Y., Shen, Y., 2016. An empirical and radiative transfer model based algorithm to remove thin clouds in visible bands. Remote Sens. Environ. 179, 183–195.
Lv, H., Wang, Y., Yang, Y., 2019. Modeling of thin-cloud TOA reflectance using empirical relationships and two Landsat-8 visible band data. IEEE Trans. Geosci. Remote Sens. 1–12.
Makarau, A., Richter, R., Muller, R., Reinartz, P., 2014. Haze detection and removal in remotely sensed multispectral imagery. IEEE Trans. Geosci. Remote Sens. 52, 5895–5905.
Makarau, A., Richter, R., Schläpfer, D., Reinartz, P., 2016. Combined haze and cirrus removal for multispectral imagery. IEEE Geosci. Remote Sens. Lett. 13, 379–383.
McCartney, E.J., 1976. Optics of the Atmosphere: Scattering by Molecules and Particles, 1976. John Wiley and Sons, Inc., New York, 421 p.
McFarquhar, G.M., Heymsfield, A.J., 1997. Parameterization of tropical cirrus ice crystal size distributions and implications for radiative transfer: results from CEPEX. J. Atmos. Sci. 54, 2187–2200.
Meyer, K., Yang, P., Gao, B.C., 2004. Optical thickness of tropical cirrus clouds derived from the MODIS 0.66 and 1.375−/spl mu/m channels. IEEE Trans. Geosci. Remote Sens. 42, 833–841.
Shen, H., Li, H., Qian, Y., Zhang, L., Yuan, Q., 2014. An effective thin cloud removal procedure for visible remote sensing images. ISPRS J. Photogramm. 96, 224–235.
Shen, Y., Wang, Y., Lv, H., Qian, J., 2015. Removal of thin clouds in Landsat-8 OLI data with independent component analysis. Remote Sens. 7, 11481–11500.
Slonecker, E.T., Jones, D.K., Pellerin, B.A., 2016. The new Landsat 8 potential for remote sensing of colored dissolved organic matter (CDOM). Mar. Pollut. Bull. 107, 518–527.
Vincent, R.K., 1972. An ERTS multispectral scanner experiment for mapping iron compounds. In: Proceedings of the 8th International Symposium on Remote Sensing of Environment, Ann Arbor, MI.
Xia, L., Zhao, F., Chen, L., Zhang, R., Mao, K., Kylling, A., Ma, Y., 2018. Performance comparison of the MODIS and the VIIRS 1.38 μm cirrus cloud channels using libRadtran and CALIOP data. Remote Sens. Environ. 206, 363–374.
Xu, M., Jia, X., Pickering, M., 2014. Automatic cloud removal for Landsat 8 OLI images using cirrus band. In: IGARSS 2014. IEEE 2014 International Geoscience and Remote Sensing Symposium, pp. 2511–2514.
Zanter, K., 2016. Landsat 8 (L8) Data Users Handbook. Landsat Science Official Website. Available online. https://landsat.usgs.gov/landsat-8-l8-data-users-handbook. accessed on 20 January 2018.
Zhang, Y., Guindon, B., Cihlar, J., 2002. An image transform to characterize and compensate for spatial variations in thin cloud contamination of Landsat images. Remote Sens. Environ. 82, 173–187.